ORIGINAL ARTICLE

Bank effects for KVLCC2

Wim Van Hoydonck[1] · Serge Toxopeus[2] · Katrien Eloot[1] · Karan Bhawsinka[2] · Patrick Queutey[3] · Michel Visonneau[3]

Abstract
A study is presented on ship–bank interaction effects in which viscous-flow solvers are used to predict the hydrodynamic forces and moments on the ship. The ship under consideration is the KRISO Very Large Crude Carrier (KVLCC2). For this hull form, Flanders Hydraulics Research (FHR) has conducted shallow water model tests in their towing tank equipped with surface-piercing banks and a vertical quay wall. The forces and moments on the KVLCC2 model were obtained for various water depths and lateral distances to the banks. Additionally, the wave elevation was measured between the quay wall and the ship model. In this study, two different CFD codes are used to predict the loads on the KVLCC2 as a function of the water depth and lateral position in the channel. The effect of propeller suction and free surface modelling on the results is quantified. Furthermore, comparisons will be made with CFD results from literature and potential flow computations to highlight the benefits of each approach. It will be shown that with careful setup of the computations, reliable predictions of the ship–bank interaction effects can be obtained.

1 Introduction

Ship–bank interaction has a strong influence on vessels sailing in waterways. It is important to account for these interaction effects in nautical training programs and in engineering analyses because interaction forces can be large and dynamic

✉ Wim Van Hoydonck
wim.vanhoydonck@mow.vlaanderen.be

Serge Toxopeus
S.L.Toxopeus@marin.nl

Katrien Eloot
katrien.eloot@mow.vlaanderen.be

Karan Bhawsinka
KBhawsinka@carnival.com

Patrick Queutey
patrick.queutey@ec-nantes.fr

Michel Visonneau
michel.visonneau@ec-nantes.fr

[1] Flanders Hydraulics Research (FHR), Berchemlei 115, 2140 Antwerpen, Belgium

[2] Maritime Research Institute Netherlands (MARIN), P.O. Box 28, 6700 AA Wageningen, The Netherlands

[3] CNRS, LHEEA Lab. (ECN/CNRS), 1, rue de la Noe, 44321 Nantes, Cedex 3, France

in nature. These effects can change abruptly and lead to a ship unexpectedly deviating from its original course and consequently, they can influence the nautical accessibility inside ports and access channels.

It is common practice to compute ship–bank interaction using model tests [4, 13, 25] or off-line computations using hydrodynamic models ranging from strip-theory-based interaction models to double-body potential flow panel methods. Tuck and Newman [23] developed two theories. First, they used slender body theory to calculate hydrodynamic interaction forces between two encountering ships moving at constant (but possibly different) velocity. In the second case, the effects of shallow water were considered when the vessels were moving with the same velocity. The developed theories gave excellent qualitative and fair quantitative agreement with experimental results. Yeung and Tan [31] investigated hydrodynamic interactions of a slow moving vessel with a coastline or an obstacle in shallow water using slender-body theory. Results were not compared with any experimental data. Pinkster and Bhawsinka [20] developed a computational procedure for the prediction of ship–ship and ship–port structure interaction using a 3D double-body potential flow method and applied it to a real-time manoeuvring simulator. It was concluded that, after tuning with model test results, the computational procedure gives

reliable values of the interaction forces enabling users of real-time simulators to simulate wider ranges of distances and speeds between passing structures. Zhou and Zou [32] use a first-order Rankine source panel method to predict the squat of a ship sailing in restricted waters. The method takes the free surface into account. To improve results, a virtual extension of the transom is generated and added to the length of the vessel. Results are compared to experimental values published in [13] and empirical formulas. The authors find that the method can be applied for ship squat prediction as long the ship is not close to the bank.

All the computational procedures listed above ignore free surface effects (except for [32]) and viscous effects while calculating interaction forces. Therefore, results from these methods start to deviate from reality at high speeds and at large drift angles [1]. Furthermore, none of these methods take into account the effect of a rotating propeller on interaction forces which are known to be significant, especially when the ship is sailing in close proximity to another structure.

More recently, attempts have been made to obtain these interaction forces using CFD computations. As CFD methods can account for free surface, viscous effects and the rotating propeller while calculating interaction forces, this seems like a logical next step. Chen et al. [2] used an unsteady chimera RANS method to study the ship–ship interaction problem in shallow and restricted waterways and validated the method against some available experimental measurements. The computed interaction forces and moments matched very well with the experimental results. They also investigated the importance of including the free surface, sinkage and trim and the influence of wall boundary conditions. Lo et al. [15] applied FLOW-3D CFD software to simulate bank effect on the KRISO 3600 TEU container ship model. Their results state that CFD modelling has achieved high precision to simulate bank effects without the need for conducting extensive model tests. Zou et al. [35], Zou [33] and Zou and Larsson [34] have done significant work in this field recently. They utilised CFD methods to investigate bank effects on a tanker moving straight ahead at low speed in a canal characterised by surface-piercing banks. Their work includes verification and validation based on a grid convergence study and comparison with experimental data, as well as the exploration of modelling error in RANS computations to enable more accurate and reliable predictions of the bank effects. In general, the CFD results of this work were considered promising and compared well with experimental data. It should be noted that Zou and Larsson [34] seem to provide the first publication where the effect of propulsion on bank suction forces were analysed using CFD. It is concluded that the propeller increases the velocity

Table 1 Main dimensions of towing tank at FHR

Total length	87.5 m
Effective length	68.0 m
Width	7.0 m
Maximum water depth	0.5 m
Length of ship models	3.5–4.5 m

around the aft-body, just like in unrestricted flow, but due to the very low velocities on the starboard (vertical wall) side, this half of the propeller gets more heavily loaded. It therefore sucks more flow on the starboard side and the reduced pressure causes a bow-out moment on the hull with the rotating propeller.

In the present paper, work performed within the AVT-216 working group of the NATO Science and Technology Organization (STO) is presented. Experiments conducted at Flanders Hydraulics Research (FHR) with a 1/75 scale model of the KVLCC2 have been reproduced with two viscous flow solvers and one potential flow solver in order to evaluate the prediction capability of these tools regarding bank effects. Earlier publications in which these FHR experiments were studied only provided a qualitative discussion on the agreement with the experiments. The present report will present quantitative comparisons with the experimental forces and moments. The effects of free surface modelling and the influence of the propeller on bank effects will be discussed to highlight modelling sensitivities in the results.

2 Experimental data

2.1 Towing tank facility

The tests with bank configuration have been carried out in May 2010 in the towing tank for manoeuvres in shallow water, located at FHR and administrated in cooperation with the Maritime Technology Division of Ghent University. A short summary of the particulars and possibilities of this towing tank [24] is given below.

2.2 Experimental setup

2.2.1 Towing tank dimensions

The main dimensions of the towing tank are listed in Table 1.

Table 2 Hydrostatic particulars of KVLCC2 (model scale) for the bank effects test program

| Parameter	Unit	Value
Length (L_{pp}, L_{oa})	m	4.2667, 4.3400
Draft Amidships (T_m)	m	0.2776 ± 0.0005
Beam (B)	m	0.7733
Longitudinal CoG (X_G)	m	0.1449 ± 0.002
Vertical CoG (KG)	m	0.2776 ± 0.0008
Displacement	m^3	0.7410 ± 0.000237
Block coefficient	–	0.8098
Mass	kg	736.2 ± 0.2
I_{XX}	kg m^2	41.0 ± 1.2
I_{YY}	kg m^2	797.3 ± 2.6
I_{ZZ}	kg m^2	831.5 ± 2.2

Fig. 1 Overview of towing tank with banks

2.2.2 Ship model

FHR owns a 1/75 scale model of the KRISO Very Large Crude carrier (KVLCC2), which was built according to the lines provided by SIMMAN (2nd variant). Consequently, its main particulars including propeller data can be found on the SIMMAN website.[1] The hydrostatic dependent particulars for the bank effects test program are given in Table 2. The vertical position of the centre of gravity of the ship is located on the waterline.

2.2.3 Bank geometry

The towing tank is equipped with a double bank configuration along the full length of the tank Fig. 1. During the tests, the ship model sails from the far side to the front of the basin. The first part of the tank that the model encounters

---
[1] http://www.simman2014.dk.
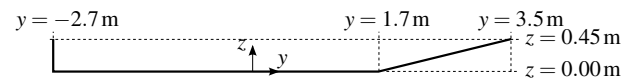
Fig. 2 Cross section of the tank geometry with vertical wall and slope

Table 3 Test conditions as a function of lateral position and depth-to-draft ratio (H/T)

H/T	− 2.1825 m	− 2.1134 m	− 1.7269 m
1.50			Case 4 (a, b)
1.35	Case 1 (a, b)	Case 2 (a, b)	Case 3 (a, b)
1.10			Case 5 (a, b)

Cases indicated with "a" are with propulsion, "b" cases without propulsion

is equipped with a 1/1 sloped wall on the negative side and a 1/3 slope on the positive side. The second section ($0 < x < 34$ m in basin coordinates) contains a vertical wall (at $y = -2.7$ m) on the negative side and on the positive side a bank with a slope of 1/4. A cross section of the configuration of the latter bank section is shown in Fig. 2.

2.2.4 Matrix of test conditions

A small subset of the KVLCC2 model test programme for bank effects executed at FHR is used as reference for the CFD computations: test results for three lateral positions at a depth $H/T = 1.35$ and for the right-most position, three H/T values (see Table 3). Only that part of the data where the vertical wall and 1/4 slope are present, is used for the current research. Negative values for the lateral positions mean that the ship is positioned towards the vertical wall. For each case, two data sets are available: (a) one with turning propeller and (b) one with stopped propeller. Propeller rpm is based on self-propulsion model point using open-water tests ($H/T \approx 1.7$). For the tests with stopped propeller, a value of 0 rpm (with an uncertainty of approximately 1 rpm) is imposed electronically. The numbering in Table 3 is used throughout this article to present data of each of the tests or computations. The model speed (reference velocity) during the experiments was $V = 0.356$ m/s, the reference length is $L_{pp} = 4.2667$ m and the average water temperature was 18.2 °C; the (speed-based) Froude number is $Fr = 0.055$ and the Reynolds number equals $Re = 1.448 \times 10^6$. The depth-based Froude numbers are 0.1897, 0.1988 and 0.2179 for the three water depths of 0.4160, 0.3744 and 0.3051 m, respectively.

2.2.5 Presentation of the results

In this study, ship-fixed forces and moments are presented. The longitudinal force X is directed forward, the transverse
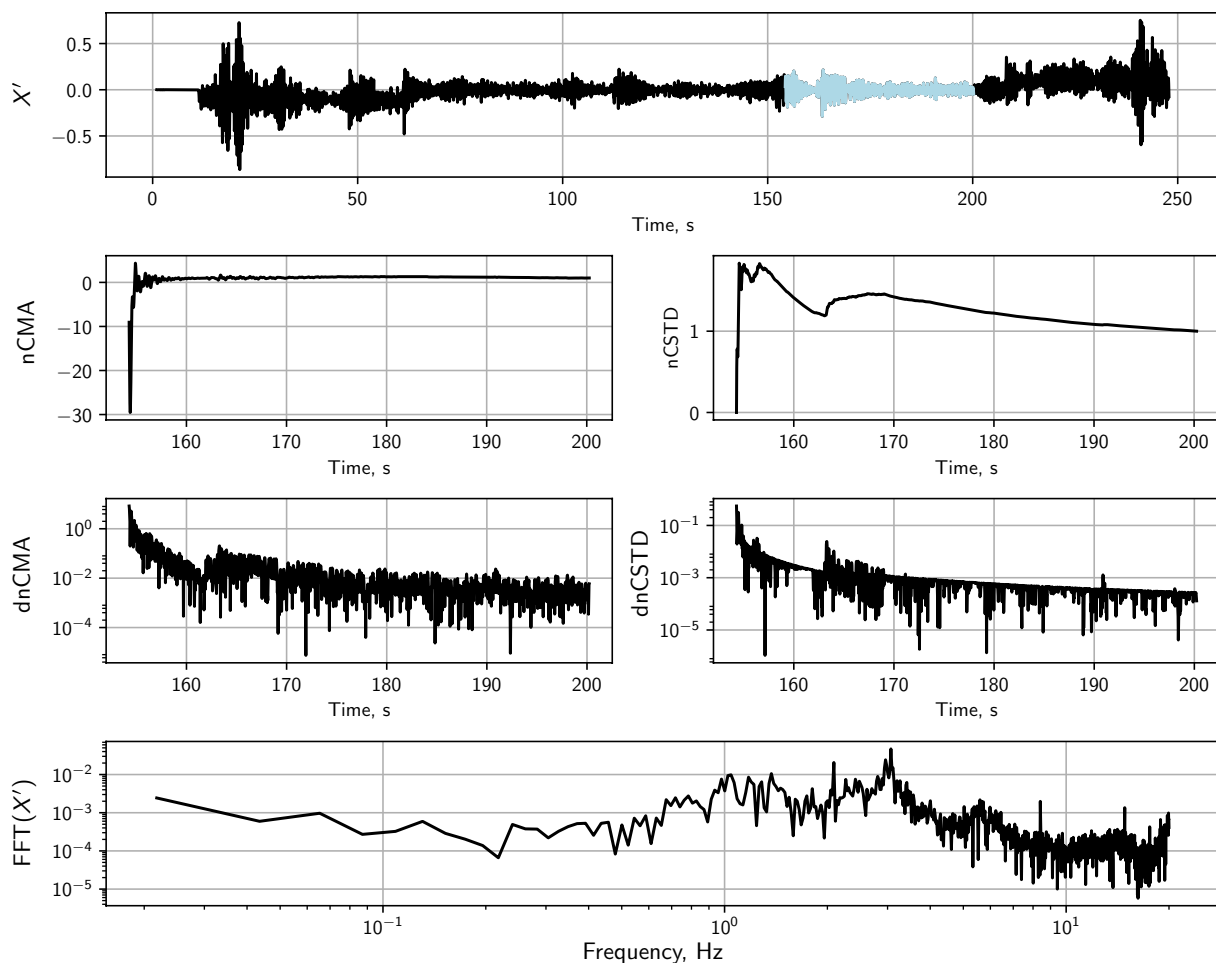
Fig. 3 Experimental data convergence analysis: X' (case 4a)

force Y is directed to starboard (i.e. positive when directed to the vertical wall), the heeling moment K is positive when pushing starboard into the water and the yaw moment N is positive when pushing the bow to starboard (i.e. towards the vertical wall). The origin of the ship-fixed axis system is located on the waterline (z), in the lateral symmetry plane of the ship (y) and amidships (x). Hull forces and moments measured during the towing tank tests and the computed forces and moments are presented as dimensionless values: forces are divided by $qL_{pp}T_m$, where q is the dynamic pressure defined as $0.5\rho V^2$. The roll moment is divided by $qL_{pp}T_m^2$ and the yawing moment is divided by $qL_{pp}^2T_m$. For the propulsive cases, thrust and torque are divided by $\rho n_p^2 D_p^4$ and $\rho n_p^2 D_p^5$, respectively, where $n_p = 5.751/s$ is the propeller rotational speed and $D_p = 0.1315 m$ is the propeller diameter.

Pressure and shear stress distributions are divided by the dynamic pressure q and non-dimensional axial velocity distributions are obtained by dividing it by the undisturbed velocity V_∞. Furthermore, the longitudinal vorticity component ω_x is made non-dimensional by L_{pp}/V_∞ and turbulent kinetic energy is divided by V_∞^2.

2.3 Analysis of experimental data

For each test case, only one experiment was executed. Hence, it is not possible to compute standard deviations for the measured values as would be the case when each experiment was repeated multiple times. To judge the steadiness of the experimental data, both the normalised cumulative moving average (nCMA) and the normalised cumulative standard deviation (nCSTD) are computed. If the derivatives of these values (dnCMA and dnCSTD, respectively) approach zero, the experimental time series converges to a steady state. In addition, the Fast Fourier Transform (FFT) of the experimental time series is computed to get an idea of the frequency content of the fluctuations.
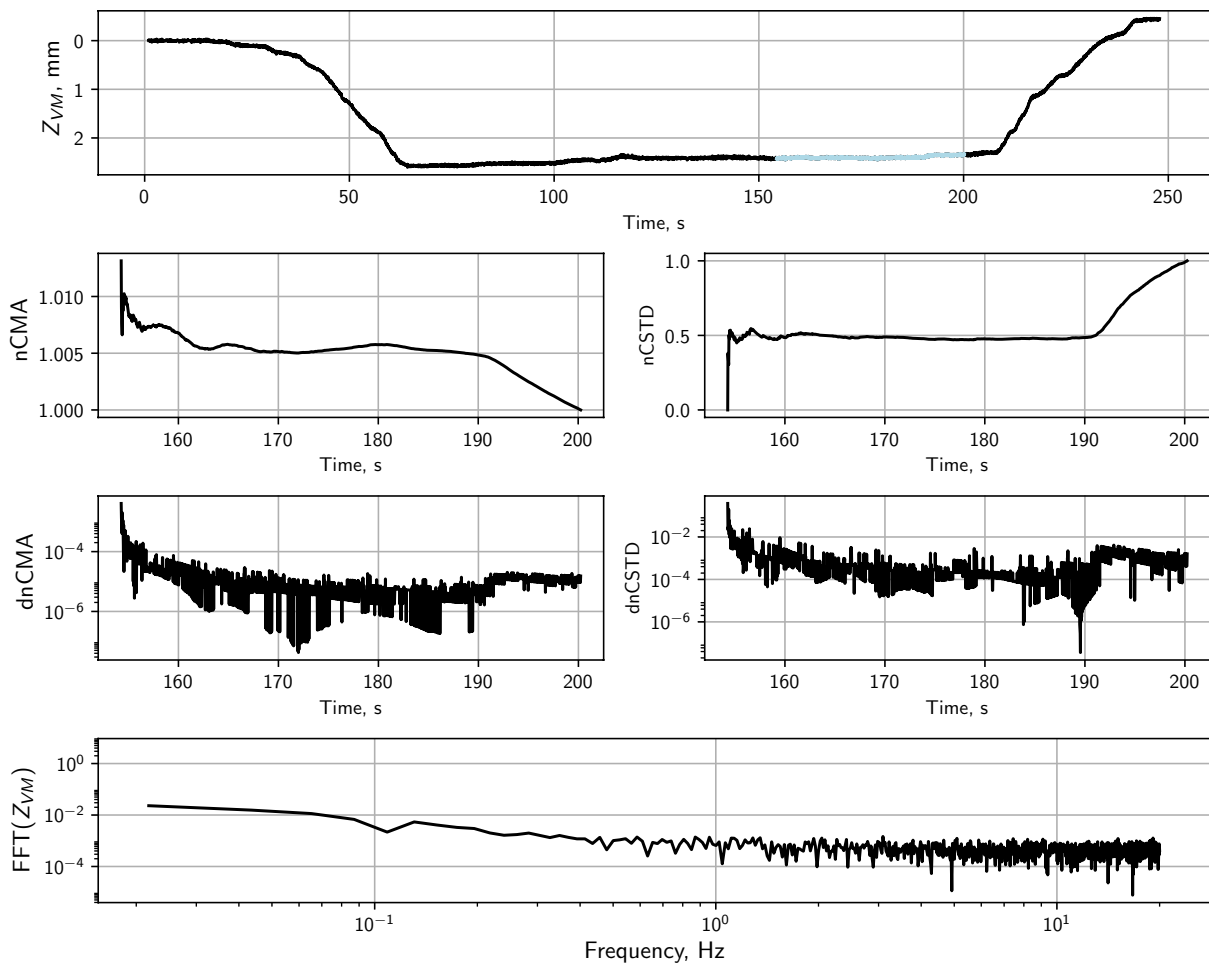
Fig. 4 Experimental data convergence analysis: midship sinkage (case 4a)

As an example, for case 4a the experimental data for X' is shown in Fig. 3. The top graph shows the measured force for the complete duration of the experiment in grey and in light blue ($\approx$ 150–200 s) the actual data that corresponds to the part during which the model passes the bank section with the vertical wall. This part of the time trace is used to compute the average values. Below this graph, the plots labelled *nCMA* and *nCSTD* show the normalised cumulative moving average and the normalised standard deviation for the light blue part. Both graphs approach one. On the third row, the plots show the numerically computed first derivatives of the figures in the second row on a logarithmic scale. These plots clearly show that both the mean and the standard deviation converge as their derivatives approach zero. On row four, the frequency content of the experimental data is shown. The frequency with the highest power is located at 3 Hz. The lowest frequency has a value that is at least an order of magnitude smaller, which indicates that the time signal does not contain a (linear) trend.

For the same test case, the sinkage at the midship location (halfway between the aft and fore perpendiculars) shows a different trend (Fig. 4). Until 190 seconds the convergence of the sinkage is very good, with differences of nCMA smaller than 1%. At this point, the sinkage starts to decrease with an almost linear trend until the end of the experimental data. This is reflected in the nCMA and nCSTD plots and their derivatives. The FFT plot on the lowest row shows that the lowest frequency signal has the highest power, which is an indication for a trend in the data. However, the measured difference in the sinkage between $t = 190$ s and $t = 200$ s is less than 0.1 mm, which is of the same order as the accuracy of the device used for the measurement of the sinkage [5].

Case 5a ($H/T = 1.1$) shows significant fluctuations in the lateral force Y', as shown in Fig. 5. Despite this, the derivatives of nCMA and nCSTD indicate that the time signal of the lateral force Y converges both in frequency and value. For this case, the dominant frequency is slightly larger than 0.2 Hz, which corresponds to the low-frequency fluctuations that are visible in the time plot.
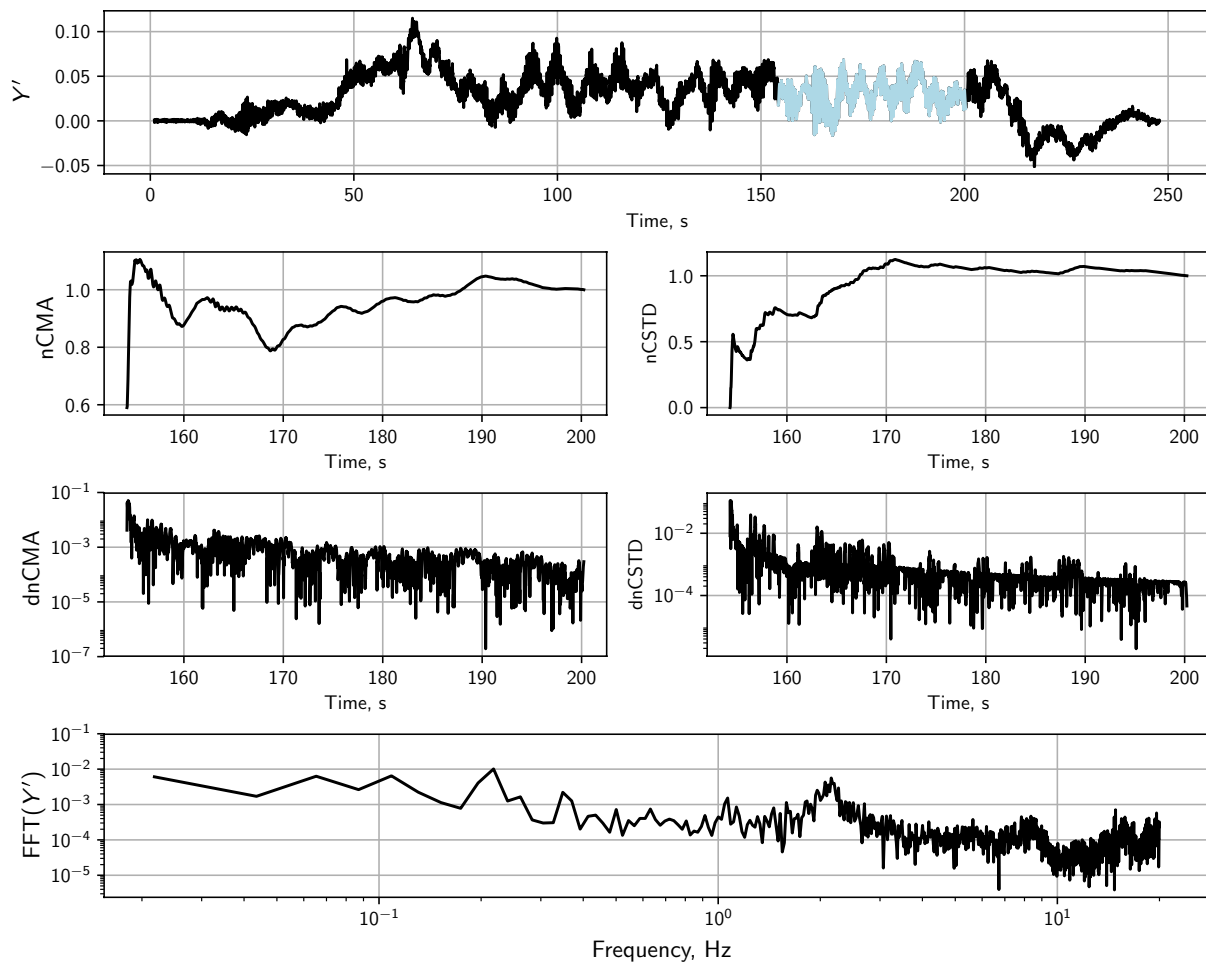
Fig. 5 Experimental data convergence analysis: lateral force Y' (case 5a)

2.4 Average values

Data averages are computed with a subset of the full test, the first 27% and the last 10% of the data is not used in the averaging process, the resulting interval from 27 to 90% corresponds to the light-blue part of the time plots as displayed in Figs. 3, 4 and 5. The average values obtained from the experiments are presented in Table 4. Note that for the cases without propulsion, thrust and torque values are not shown, although these values were measured as well. All values are rounded to four significant digits.

2.5 Water surface elevation

Data from multiple wave gauges were recorded during the experiments. One of these gauges is located halfway between the beginning and the end of the bank configuration, between the vertical wall and the ship, at a longitudinal position of $x_{wg} = 19$ m. Its lateral position in the tank is $y_{wg} = -2.68$ m. Hence, there is a gap of two centimetres

between the vertical wall and the wave measurement device, as the vertical wall is located at $y = -2.7$ m (as shown in Fig. 2). For computations where the free surface is taken into account, these water surface elevation measurements can be used to validate the prediction of the free surface position. The waiting interval between tests was 2000 s long. Conversion of the position of the wave gauge to a ship-fixed coordinate system is done as follows:

$$x_{wg,rel} = \frac{x_{ship} - x_{wg}}{L_{pp}} \tag{1}$$

where x_{ship} is the longitudinal position of the midship location in the towing tank coordinate system. The converted wave measurements are shown in Fig. 6 for the cases with and without propulsion, positive x-coordinates correspond to positions ahead of the midship location, and positive y-coordinates correspond to an increase in water surface height.

For all cases, an upward peak is observed when the ship bow passes the wave gauge. The peak value is inversely

Table 4 Average values obtained from the measurements

	Cases 1a–5a (with propulsion)				
	1a	2a	3a	4a	5a
X'	− 0.02701	− 0.01700	− 0.007073	− 0.003843	− 0.02344
Y'	0.1087	0.1134	0.04782	0.04316	0.02994
K'	0.02334	0.02235	0.01012	0.004497	0.01851
N'	− 0.007405	− 0.01131	− 0.004165	− 0.003371	− 0.01501
K_T	0.2445	0.2524	0.2280	0.2392	0.2626
K_Q	0.03057	0.03622	0.03257	0.03411	0.03559
Sinkage, mm	3.620	3.558	2.783	2.397	3.977
Trim, deg	− 0.03759	− 0.03459	− 0.03180	− 0.02849	− 0.04049
	Cases 1b–5b (without propulsion)				
	1b	2b	3b	4b	5b
X, N	− 0.05058	− 0.04630	− 0.03346	− 0.03237	− 0.04912
Y, N	0.08023	0.06349	0.03042	0.02569	0.01052
K, Nm	0.02810	0.01325	0.006753	0.005893	0.01928
N, Nm	− 0.002928	− 0.002910	− 0.002895	− 0.001056	− 0.01621
Sinkage, mm	3.356	3.229	2.738	2.201	3.714
Trim, °	− 0.04302	− 0.03945	− 0.03449	− 0.03136	− 0.04521

(a) With propulsion

(b) Without propulsion
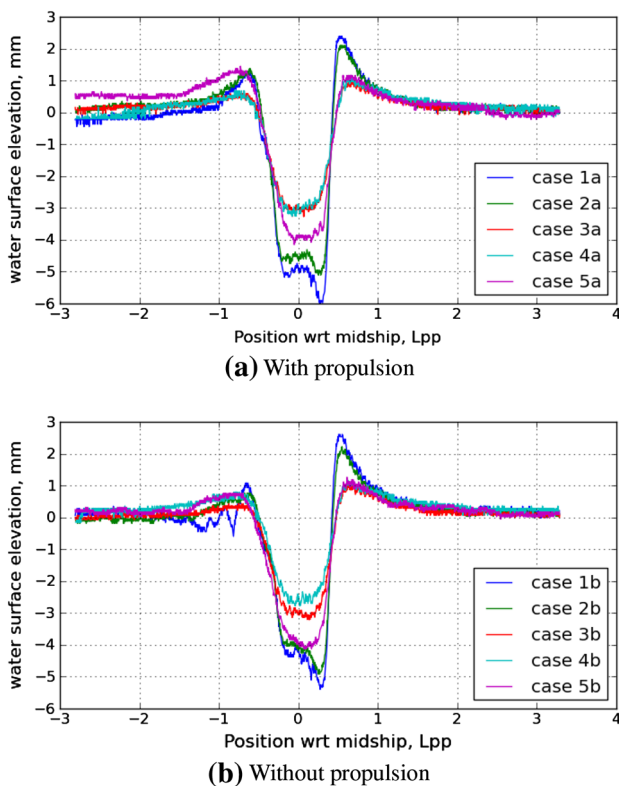
Fig. 6 Measured wave elevations at wave gauge 5

proportional to the lateral distance to the quay; for cases 3, 4 and 5 the peak value is the same. Between the ship and the quay, the depression is more pronounced as the ship sails closer to the quay, but here, also the depth value has an influence on the maximum depression. For cases 1 and 2 (both a and b), the depression is not symmetric with respect to the ship length, but shows a peak near $L_{pp}/4$ ahead of the midship location. Case 5a is the only one for which the peak in water surface elevation near the aft perpendicular is higher than the peak at the bow.

3 Computational setup

3.1 REFRESCO

REFRESCO is a viscous-flow CFD code that solves multiphase (unsteady) incompressible flows with the RANS equations, complemented with turbulence closure models, cavitation models and volume-fraction transport equations for different phases [27]. The equations are discretised using a finite-volume approach with cell-centred collocated variables and in strong-conservation form. A pressure-correction equation based on the SIMPLE algorithm is used to ensure mass conservation [11]. Time integration is performed implicitly with first or second-order backward schemes. At each implicit time step, the non-linear system of velocity and pressure is linearised with Picard's method and either a segregated or coupled approach is used. In the latter, the coupled linear system is solved with a matrix-free Krylov subspace method using a SIMPLE-type preconditioner [11]. A segregated approach is always adopted for the solution of all other transport equations. The implementation is face-based,
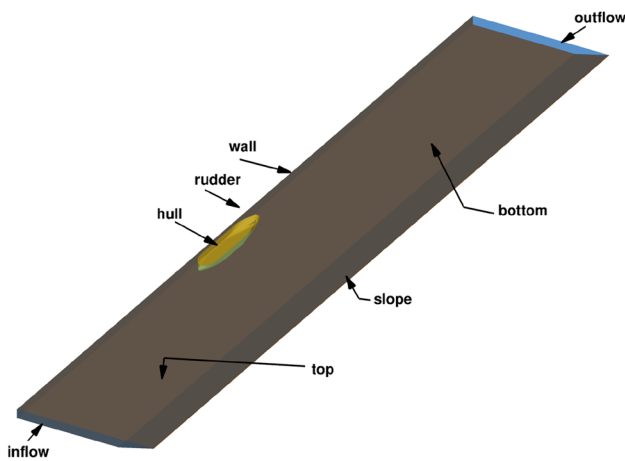
Fig. 7 Domain for REFRESCO computations

permitting unstructured grids with elements consisting of an arbitrary number of faces (hexahedra, tetrahedra, prisms, pyramids, etc.). State-of-the-art CFD features such as moving, sliding and deforming grids, as well automatic grid refinement are also available in the code.

For turbulence modelling, RANS/URANS, Scale Adaptive Simulation (SAS) [16], ((I)D)DES, Partially Averaged Navier Stokes (PANS) and LES approaches are available [18]. The Spalart correction [3] to limit the production of turbulence kinetic energy based on the stream-wise vorticity can be activated. Automatic wall functions are available.

The code is parallelised using MPI and sub-domain decomposition, and runs on Linux workstations and HPC clusters. REFRESCOis currently being developed, verified and validated at MARIN in the Netherlands in collaboration with IST (Lisbon, Portugal), USP-TPN (University of São Paulo, Brazil), Delft University of Technology, the University of Groningen, the University of Southampton, the University of Twente and Chalmers University of Technology.

3.2 Computational domain and setup

Due to the different water depths and distances of the ship to the vertical wall, separate grids had to be made for each case. Free surface deformation was not taken into account in the REFRESCOcomputations. To account for the dynamic trim and sinkage the experimental values were applied in the grid generation. This means that also for the cases with and without propulsion, separate grids had to be generated. To ensure grid similarity between the cases and between different grid densities, the meshing process was automated using scripts. Unstructured grids with hexahedral elements were generated using HEXPRESS. At the hull and rudder surfaces, an inflation layer was added to be able to capture the high gradients in the boundary layer.

**Table 5** Grid densities for REFRESCO grid sensitivity study, case 1b

Grid Id	Number of cells n_c	Faces on hull surface	y^+_{max} on hull surface
Coarse	2,922,462	31,750	0.51
Medium	4,523,429	45,467	0.46
Fine	7,449,527	68,385	0.34
Very fine	11,453,879	96,743	0.33
Extremely fine	26,174,442	183,077	0.25
Ultimately fine	34,731,429	228,742	0.23

The inlet and outlet boundaries were located at $4L_{pp}$ forward and $4L_{pp}$ aft of the aft perpendicular of the ship. In Fig. 7 the domain and boundary definitions are shown. Symmetry boundary conditions were applied on the undisturbed water surface (top). On the hull and rudder surface, no-slip and impermeability boundary conditions are used ($\overline{u} = 0$). Due to the application of the inflation layer at these surfaces, the y^+_{max} values are around 0.5 and therefore the boundary layer is resolved down to the wall. On the vertical wall, on the slope and on the bottom surface, the boundary condition is set to moving wall/fixed slip ($\overline{u} = \overline{V_\infty}$ with V_∞ the inflow velocity). At these boundaries wall functions are used to avoid large grid densities. A pressure boundary condition is applied at the outflow and inflow boundary conditions at the inflow. The inflow turbulence intensity is set to 1% and the eddy viscosity at the inflow to $\mu_t = 1\mu$. All calculations were conducted for a Reynolds number $Re = 1.5 \times 10^6$. The REFRESCO calculations presented in this study were all conducted without incorporating free-surface deformation and assuming steady flow, unless stated otherwise. The $k - \omega$ SST model [17] was used as turbulence closure. For the a cases, the propeller action was achieved by coupling REFRESCO with the potential flow code PROCAL [26] and using the obtained forces on the propeller as body forces in the viscous-flow computation [22]. In the propelled cases, the propeller rotational speed was set to 345.3 min^{-1} and the propeller thrust was obtained from the computation. For the b cases, the stopped propeller was not considered in the computations.

3.3 Solution verification

To obtain information about the sensitivity of the solutions to the grid density, a series of grids with various densities was generated for case 1b. Each grid was made using identical levels of refinements. The grid density was controlled by adjusting the number of cells in the initial base mesh. To maximise the grid similarity between different grid densities, the refinement diffusion was increased when increasing

Fig. 8 Case 1b: solution verification for REFRESCO (top: iterative convergence, bottom: grid sensitivity)
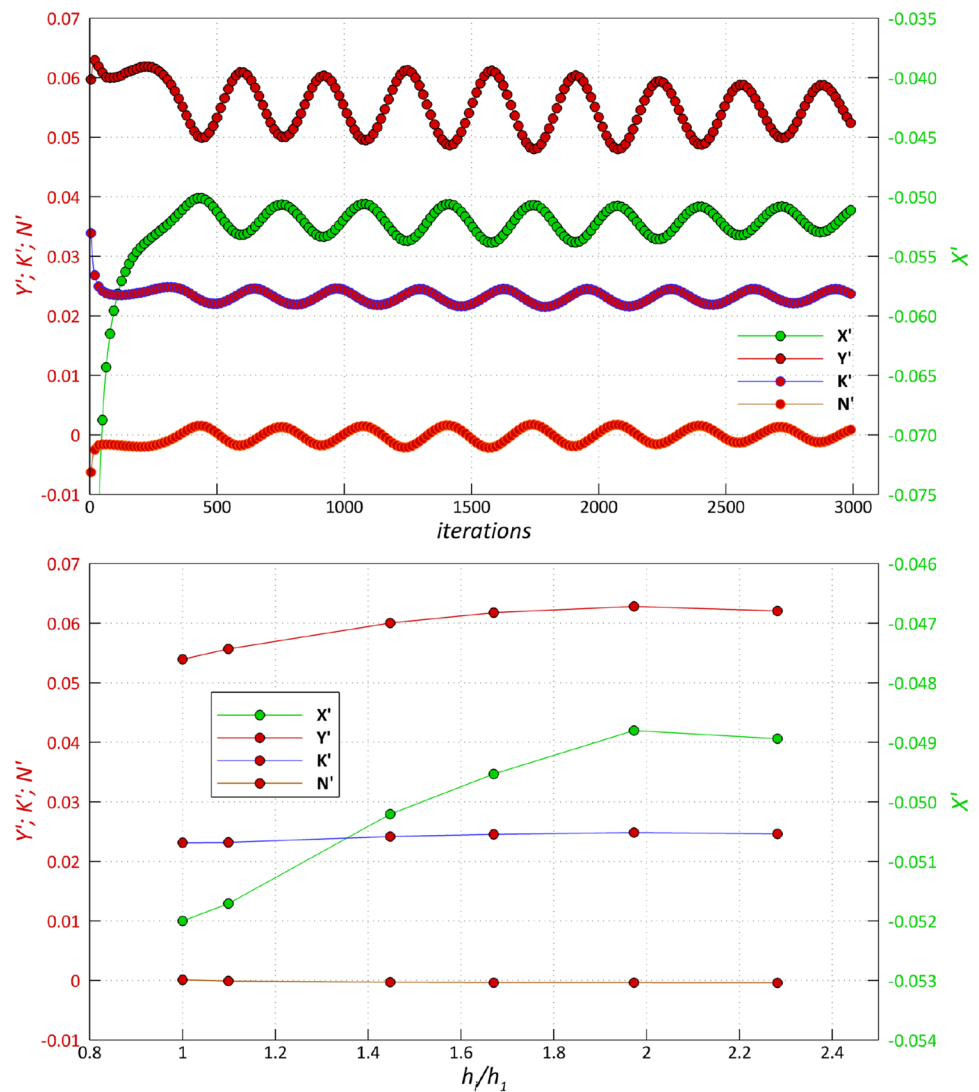
the grid density. For the hull and rudder surface, the first cell height was adjusted as a function of the density as well. Unfortunately, the way in which HEXPRESS generates the inflation layer does not allow users to fully control the mesh similarity close to walls. This means that upon grid refinement, the inflation layer becomes thinner and eventually, extrapolation to an infinitely fine grid would result in a solution on a grid without inflation layer. Therefore, a formal uncertainty estimate based on geometrically similar grids cannot be made. The study presented should therefore be considered as a grid sensitivity study. The grid sizes that were investigated are shown in Table 5.

For the finest grid (*ultimately fine*), the iterative convergence for case 1b is shown by the left graph in Fig. 8. The convergence shows a clear oscillation of the forces (standard deviation of 1.6% in X and 6.6% in Y) and moments (standard deviation of 4.0% in K and 0.3 Nm in N, which is larger than the mean value) and the uncertainty in the solution

due to the iterative process can therefore not be neglected. This means that the discretisation error will be contaminated by scatter due to insufficient iterative convergence [8]. All computations have been conducted assuming steady flow, but the oscillatory behaviour of the global quantities during the iterative process in each case indicates that unsteady effects may be present in the flow and an unsteady solution approach may be more appropriate. In the remainder of this article, the forces and moments shown will be based on an average of the last part of the convergence history for each case.

In graph on the right of Fig. 8, the integral results for case 1b for the various grid densities are shown. On the horizontal axis, the relative step size $h_i/h_1 = \sqrt[3]{n_{c,1}/n_{c,i}}$ is shown. A relative step size of 1 represents the result for the finest grid, while larger values correspond to coarser grid results. A formal uncertainty estimate (e.g. following [9]) could not be made due to apparent divergence of the results upon grid refinement,
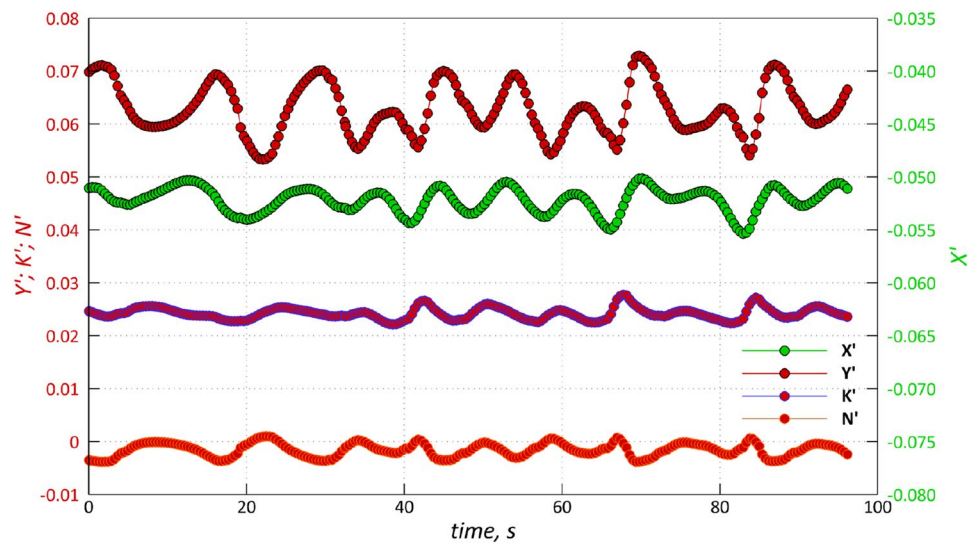
Fig. 9 Case 1b: unsteady solution for RеFRESCO

Table 6 Comparison between steady and unsteady computation results, RеFRESCO, case 1b

Result	Δt, s	X'	Y'	K'	N'	Time on 300 CPUs, h
		$\times 10^3$	$\times 10^3$	$\times 10^3$	$\times 10^3$	
Steady	–	− 51.8	57.5	24.046	− 0.56	2
Unsteady	0.02	− 52.2	62.7	24.046	− 1.56	150
EFD	–	− 50.6	80.2	27.893	− 2.94	–

leading to unrealistically high uncertainty estimates. From the results, it can be concluded that even for the finest grids the solution still changes and even finer grids should be used in order to avoid too large uncertainties in the results due to discretization errors. This conclusion confirms the observations by Zou and Larsson [34] in which also large uncertainties (e.g. a numerical uncertainty in Y of more than 24% of the solution on the finest grid) were found for bank-effects computations.

In the graphs presented in this article regarding the trends of bank suction effects, RеFRESCO results for the *medium* grid are included. Based on the solution verification, it is found that the numerical uncertainty in the results is rather large and therefore it will be hard to draw quantitative conclusions on the accuracy of the modelling approach. Any deviations from the true value can be caused by either modelling errors, or due to uncertainties in the solutions. In future studies, finer grids and probably an unsteady solution approach should be adopted to better quantify the trends. To investigate the influence of time on the solution, an unsteady computation has been performed. The results are presented below.

3.4 Unsteady solution

A preliminary study has been done in order to quantify the effect of an unsteady solution method compared to steady

computations. For the finest grid, i.e. 35 million grid points, a computation with second order time discretization was performed with a time step of 0.02 s = 1/600 L_{pp}/V and desired normalised RMS residual convergence level per time step of $L_2 < 5 \times 10^{-5}$. The computation was restarted from a computation with coarser time step (0.1 s) and ran 4810 time steps, or 96.2 s. On average, about 25 outer loops per time step were required to reach the desired iterative convergence. The forces and moments as a function of time are shown in Fig. 9. This figure clearly shows the unsteady nature of the flow. Surprisingly, the loads do not converge towards an harmonic signal and even after 96 s, statistical convergence is not obtained. It should be noted that these 96 s are much longer than the time during which the model was sailing in the section with the vertical bank during the experiments, and significantly longer than the time over which the average of the experiments was taken.

A comparison of the forces and moments obtained with the steady computation and the unsteady one are given in Table 6. The result of the unsteady computation are very similar to those obtained with the coarser time step of 0.1 s and therefore the discretization error in time appears to be small. Although for Y and N a very small improvement compared to the experiment appears to be made, a significant difference still remains. Since the computing time for

Fig. 10 Case 1b: steady (top) and time-averaged unsteady (bottom) wake field for REFRESCO
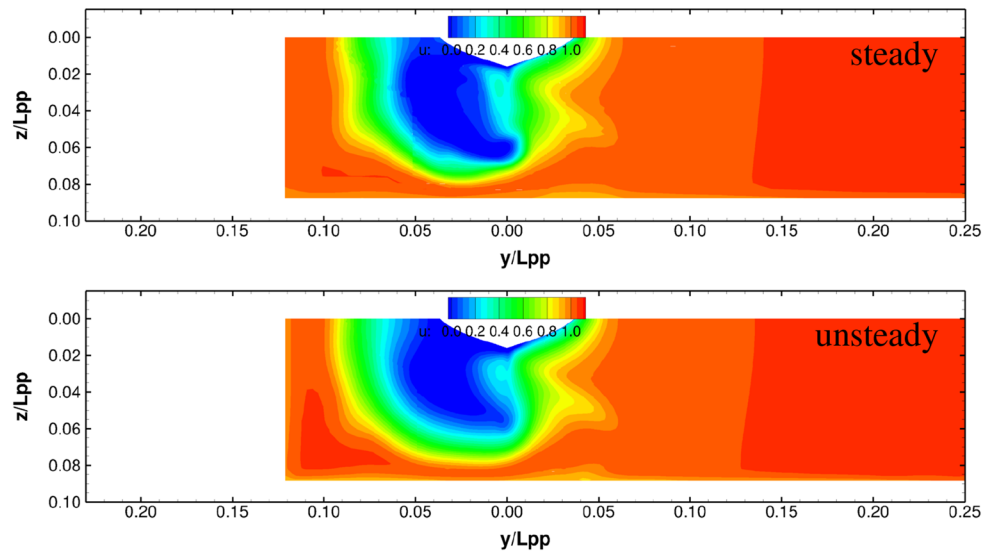
the unsteady calculation is 75 times larger than the steady one, the marginal improvement does not seem to justify the additional computational effort.

To investigate whether the time-averaged unsteady computation produces a wake that is similar to the wake obtained with the steady computation, Fig. 10 is made. In this figure, some differences can be seen, but the overall flow features do not appear to change much between the steady and unsteady cases.

3.5 ROPES

ROPES has been developed for the prediction of ship–ship interaction forces in shallow water of arbitrary depth. The computational method used in ROPES is based on three-dimensional potential flow and the double-body assumption. This means that free-surface effects of vessels are not accounted for. Furthermore, trailing wakes are not implemented in ROPES, so the potential flow model does not include lift effects. The flow equations are solved using standard zero-order panels and Rankine sources with or without the effect of restricted water depth and channel walls [12, 19]. Based on the solution of the source strength on the panels describing the bodies, the hydrodynamic forces on the ships are computed based on equations developed by Xiang and Faltinsen [30]. These equations are used to compute the complete set of hydrodynamic forces on all bodies. ROPES is applicable to multi-body simulation scenarios involving various ships and port structures.

A close-up view of the panel distribution on the hull and on a part of the vertical wall is given in Fig. 11. The vertical wall extends from $x/L_{pp} = -4$ to $x/L_{pp} = 4$. The hull is represented using 2438 panels, while 2184 panels are used to describe the vertical and sloped wall. Since ROPES cannot handle lifting surfaces, the rudder has been removed from

the ship geometry. The computations were executed at full scale conditions and the resulting forces and moments were converted to model scale.

3.6 ISIS-CFD

The ISIS-CFD solver that is part of the FINE/Marine CFD computing suite, is an incompressible, unsteady, Reynolds-averaged Navier–Stokes (URANS) solver mainly devoted to marine hydrodynamics. The solver features several sophisticated turbulence closure models: apart from the classical two-equation $k - \epsilon$ and $k - \omega$ models, the anisotropic two-equation Explicit Algebraic Stress Model (EASM), as well as Reynolds Stress Transport Models, are available with or without rotation corrections [7]. All turbulence models are compatible with wall-function or low-Reynolds near wall formulations. Hybrid LES turbulence models based on Detached Eddy Simulation (DES) are also implemented and are validated on automotive flows characterised by large
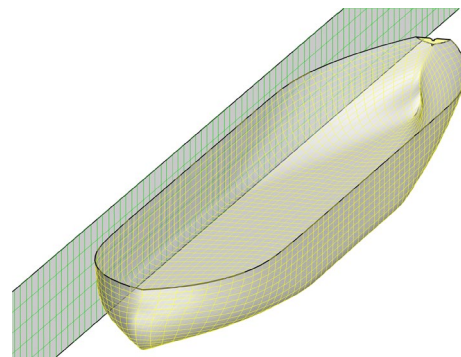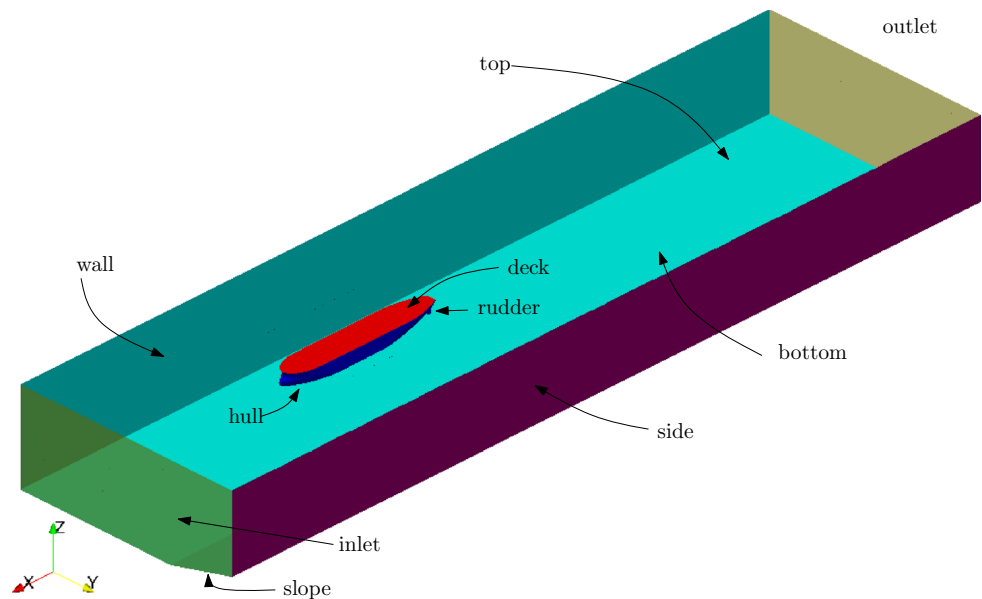

Fig. 11 Panel distribution on hull and part of the vertical wall for ROPES computations

Fig. 12 Domain for ISIS-CFD computations

separations [10]. Additionally, several cavitation models are available in the code.

The solver is based on the finite volume method to build the spatial discretization of the transport equations. The unstructured discretization is face-based. While all unknown state variables are cell-centred, the systems of equations used in the implicit time stepping procedure are constructed face by face. Fluxes are computed in a loop over the faces and the contribution of each face is then added to the two cells next to the face. This technique poses no specific requirements on the topology of the cells. Therefore, grids can be completely unstructured: cells with an arbitrary number of arbitrarily-shaped faces are accepted. Pressure-velocity coupling is enforced through a Rhie and Chow SIMPLE type method: at each time step, the velocity updates come from the momentum equations and the pressure is given by the mass conservation law, transformed into a pressure equation. In the case of turbulent flows, transport equations for the variables in the turbulence model are added to the discretization. Free-surface flow is simulated with a multi-phase flow approach: the water surface is captured with a conservation equation for the volume fraction of water, discretized with specific compressive discretization schemes [21]. The technique included for the 6 degrees of freedom simulation of ship motion is described by Leroyer and Visonneau [14]. Time-integration of Newton's law for the ship motion is combined with analytical weighted or elastic analogy grid deformation to adapt the fluid mesh to the moving ship. To enable relative motions of appendages, propellers or multiple bodies, both sliding and overlapping grid approaches have been implemented. Various options are available in ISIS-CFD to take propulsive effects into account: propellers can be modelled using actuator disc theory, by coupling

with boundary element codes (RANS BEM coupling [6]), or by direct discretization through e.g. rotating frame method or sliding interface approaches. Finally, a anisotropic automatic grid refinement procedure has been developed which is controlled by various flow-related criteria [28].

Parallelization is based on domain decomposition. The grid is divided into different partitions; these partitions contain the cells. The faces on the boundaries between the partitions are shared between the partitions; information on these faces is exchanged with the MPI (Message Passing Interface) protocol. This method works with the sliding grid approach and the different sub-domains can be distributed arbitrarily over the processors without any loss of generality. Moreover, the automatic grid refinement procedure is fully parallelized with a dynamic load balancing algorithm that works transparently with or without sliding grids.

3.6.1 Computational domain and setup

The computational domain with boundary conditions is shown in Fig. 12. The top of the domain is located $0.5L_{pp}$ above the water surface. At this surface, the pressure is prescribed using the *Updated hydrostatic pressure* boundary condition of ISIS-CFD. The inlet is located $1.5L_{oa}$ ahead of the bow of the ship, and the outlet is located $2.5L_{oa}$ aft of the stern, hence the total domain length is approximately $5L_{oa}$. For both of these surfaces, a far-field boundary condition is applied ($V = V_\infty$). The bottom and the surface-piercing tank walls are modelled as solid walls having a relative velocity with respect to the ship. Wall function boundary conditions are applied at these surfaces. A no-slip condition is applied to the rudder surfaces and the hull except for the deck, where a slip condition is applied. The lateral wall on port side has

Table 7 Grid sizes for the computations of FHR

Case id	Number of cells n_c
case 1a,b	15,638,287
case 2a,b	15,569,011
case 3a,b	16,843,438
case 4a,b	17,086,694
case 5a,b	15,855,507

Table 8 Grid densities for ISIS-CFD grid sensitivity study, case 1b

Grid id	Number of cells n_c	Faces on hull surface	y^+_{max} on hull surface
Very coarse	3,595,215	86,302	1.08
Coarse	7,180,624	158,641	0.87
Medium	9,888,790	207,245	0.75
Fine	15,638,287	319,748	0.52

a slip condition as well. No wall functions are used on the the hull and rudder surfaces, i.e. the flow is resolved down to the wall ($y^+_{max} \approx 0.5$).

Propulsion is modelled using an actuator disk, for which the measured thrust and torque values are used as input (see Table 4). This method requires extra grid refinements near the propeller location. The same grids are used for the propulsive cases and the non-propulsive cases, hence five meshes are generated. For each combination of lateral position and water depth, first a computation without propulsion is executed after which the propulsive cases are computed using the solution of the non-propulsive case as initial condition. For the non-propulsive cases, the stopped propeller is not taken into account.

Trim and sinkage are solved for in the ISIS-CFD computations. To ensure that due to sinkage, the cells below the hull are not compressed too much (which may result in negative cell volumes), the hull is meshed 3 mm below the hydrostatic position. Vertically, the centre of gravity is located on the waterline. Longitudinally, it is located 0.1482 m ahead of the midship location. This value is approximately 2 mm aft of the longitudinal location of the centre of gravity as recorded in the experiments (see Table 2). For each case the grid contains approximately 16×10^6 cells, the actual numbers are documented in Table 7.

Initially, all computations were run using a first-order time discretization scheme that uses a quasi-static approach to update the attitude and vertical position of the ship such that the resulting accelerations approach zero. For case 1b, a second-order time discretization scheme—where Newton's laws are tightly coupled to the flow motion at each time step—has been used as well.[2] For this case, the inertia moments of the ship hull are required as input. In the analyses that follow, the ISIS-CFD computations using a first-order time discretization are labelled *ISIS-CFD*, whereas the computation that uses a second-order time discretization is labelled *ISIS-CFD unsteady*.

3.6.2 Solution verification

For case 1b, additional grids were generated for solution verification. The cell sizes were modified by adjusting the cells

sizes in the initial Cartesian grid. For example, the *medium* mesh was generated by increasing the linear dimensions of the initial cells by a factor 1.25. Furthermore, for refinement surfaces and refinement boxes with absolute target cell sizes (such as the surfaces used for water surface refinement), the target cell size values were multiplied by this refinement factor as well. For the hull and rudder, the first cell size was adjusted (increased) as well, resulting in lower y^+ values for the finer meshes (as shown in Table 8).

The iterative convergence on the fine grid (left) and the values of the integral quantities obtained on the four grids (right) are shown in Fig. 13. Similar to the solution verification of REFRESCO (Sect. 3.3), the horizontal axis of the right-hand graph in this figure shows the relative step size $h_i/h_1 = \sqrt[3]{n_{c,1}/n_{c,i}}$: the finest grid has a relative step size of one. These results show that the iterative convergence for ISIS-CFD is good, especially when compared to the iterative convergence of REFRESCO (shown earlier in Fig. 8). For the longitudinal force X grid convergence is oscillatory. On the finest grid, the lateral force Y shows a very slight divergent trend. Although integral values do not change very much between the fine and medium mesh, a finer grid should be used to verify that the finest mesh used here is sufficient.

3.6.3 Adaptive grid refinement

For case 3b, ECN/CNRS performed a computation using ISIS-CFD with adaptive grid refinement (AGR) starting from a steady solution obtained on a coarse mesh (with approximately 5×10^6 cells) that was provided by FHR. A new combined refinement criterium for both the free-surface and the vortical structures has been used [29]. The minimum size limit for refined cells has been retained to 0.002 m and is activated each 50 steps of the time marching procedure in order to find a steady solution. This leads to a refined grid of about 20×10^6 cells.

3.7 Overview of computational settings

For the five test cases without propulsion, results from [35] will be included in the comparison between CFD predictions and the experiments. A summary of the settings for

---

[2] Due to time constraints, not all cases could be run in this mode.

Fig. 13 Case 1b: solution verification for ISIS-CFD, (top: iterative convergence on fine grid, bottom: grid sensitivity)

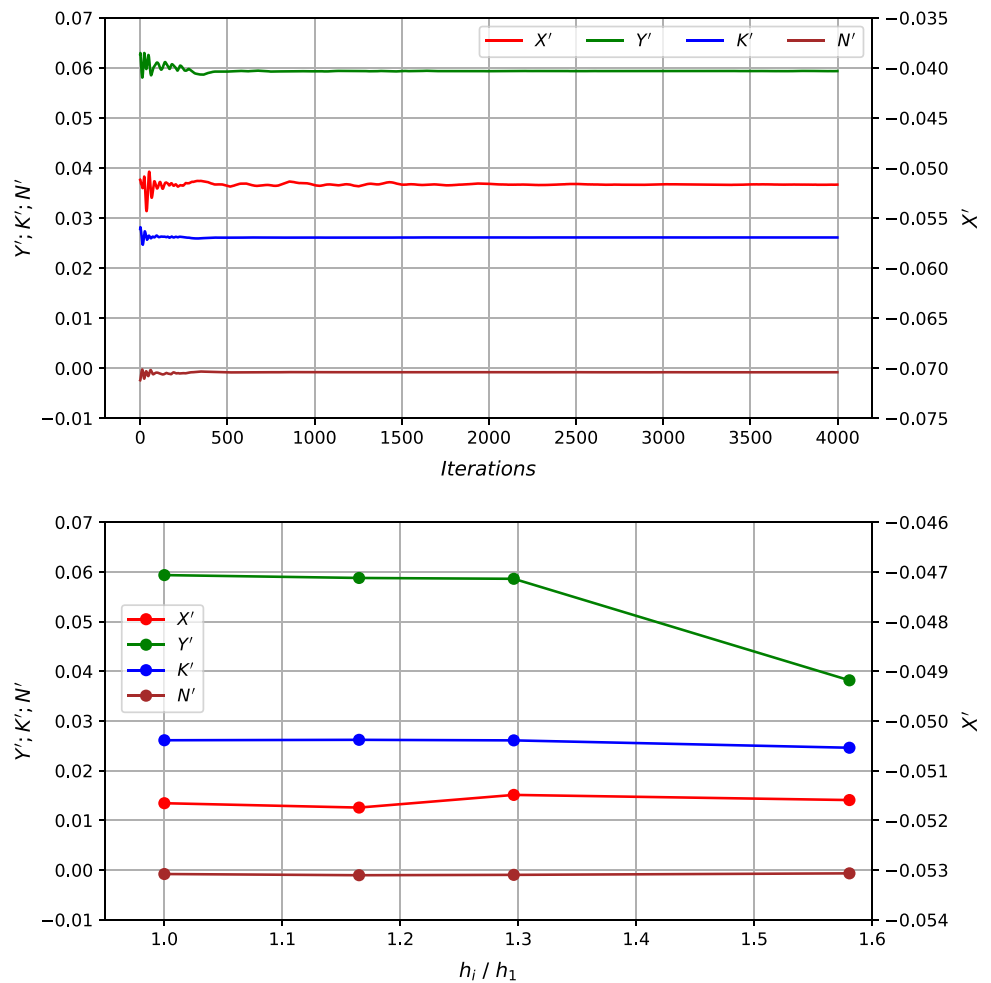**Table 9** CFD computation settings

	Turbulence model	y^+	Free surface	Time discr. order	Space discr. order	Propeller (a cases)	Propeller (b cases)	Approx. mesh sizes
ISIS-CFD	EASM	< 0.5	VOF	1st	2nd	Actuator disc	–	16×10^6 (incl. air)
ISIS-CFD (AGR)	EASM	< 0.5	VOF	1st	2nd	–	–	20×10^6 (incl. air)
ISIS-CFD (unsteady)	EASM	< 0.5	VOF	2nd	2nd	–	–	16×10^6 (incl. air)
ReFRESCO	$k - \omega$ SST	< 0.5	No	–	2nd	BEM coupling	–	5×10^6
SHIPFLOW [34]	$k - \omega$ SST	< 1.0	No	–	2nd	–	No slip surface	2×10^6 (overset)

the computations used in the force and flow field comparisons as discussed later in this report is given in Table 9.

4 Comparison of global forces and moments

The computed global forces and moments will be compared with the experimental data both on an absolute and relative scale. For the absolute comparisons (Figs. 14, 15),

the non-dimensional values are used as-is. For relative comparisons (Fig. 16), the experimental results are used as a reference and for each CFD result, the comparison error is computed as follows,

$$E(\%D) = \frac{S - D}{D} \times 100, \qquad (2)$$

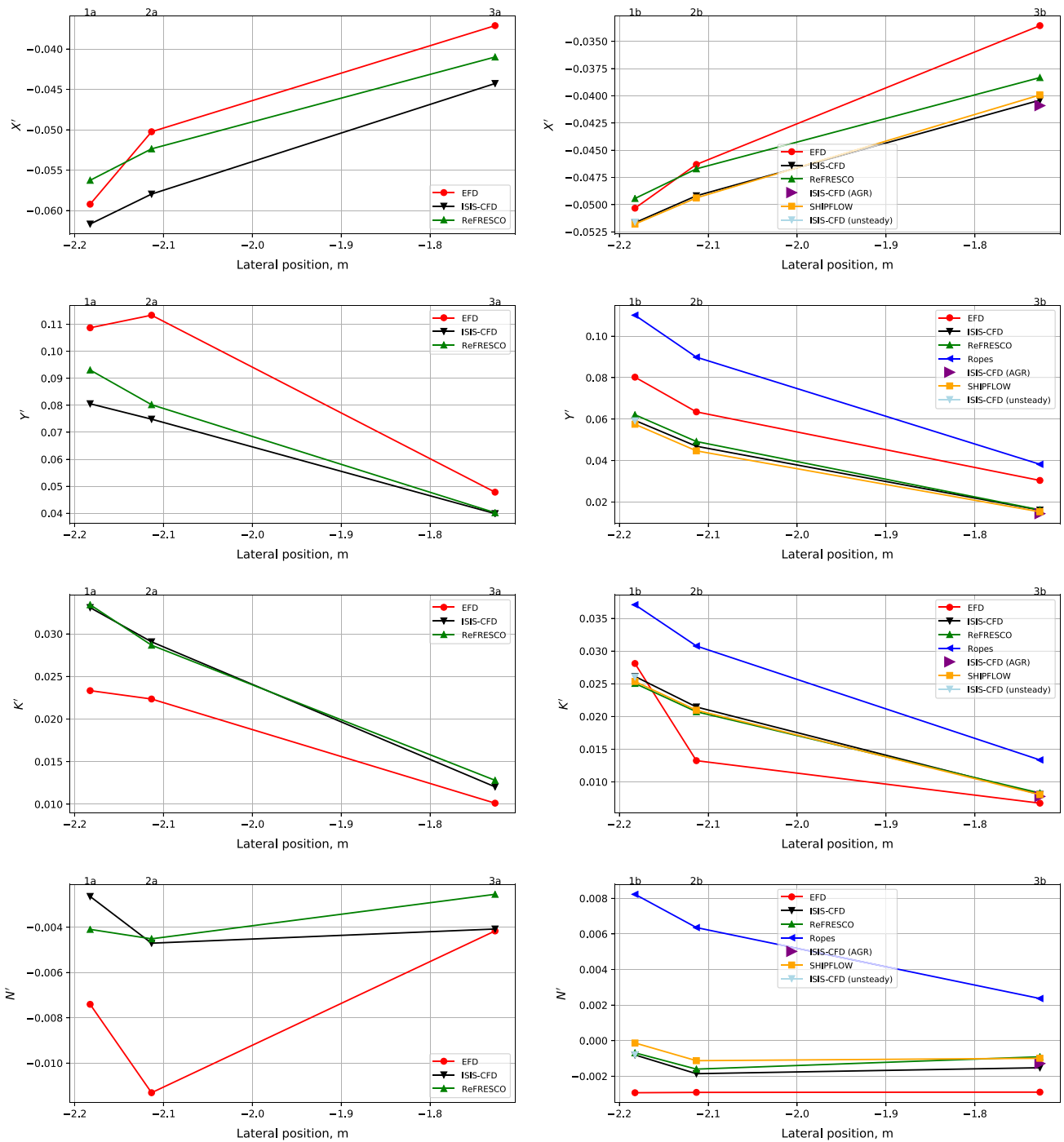where S is the numerical result and D the experimental reference value.

Fig. 14 Resulting forces and moments as a function of lateral distance to the quay (left: with propulsion, right: without propulsion)

The integral quantities that are compared are the resultant longitudinal force X, the lateral force Y, the roll moment K and the yawing moment N. For the X-axis of plots, the lateral position of the ship in the tank (cases 1, 2 and 3) and under keel clearance (cases 3, 4 and 5) is used. Hence, two sets of plots are created with the third case appearing in both. For all of these, separate plots will be made for the a and b cases (with and without propulsion, respectively). Afterwards, the computed thrust values will be compared with the experimental data. In all figures that show absolute values, the case names are shown above the plot area.
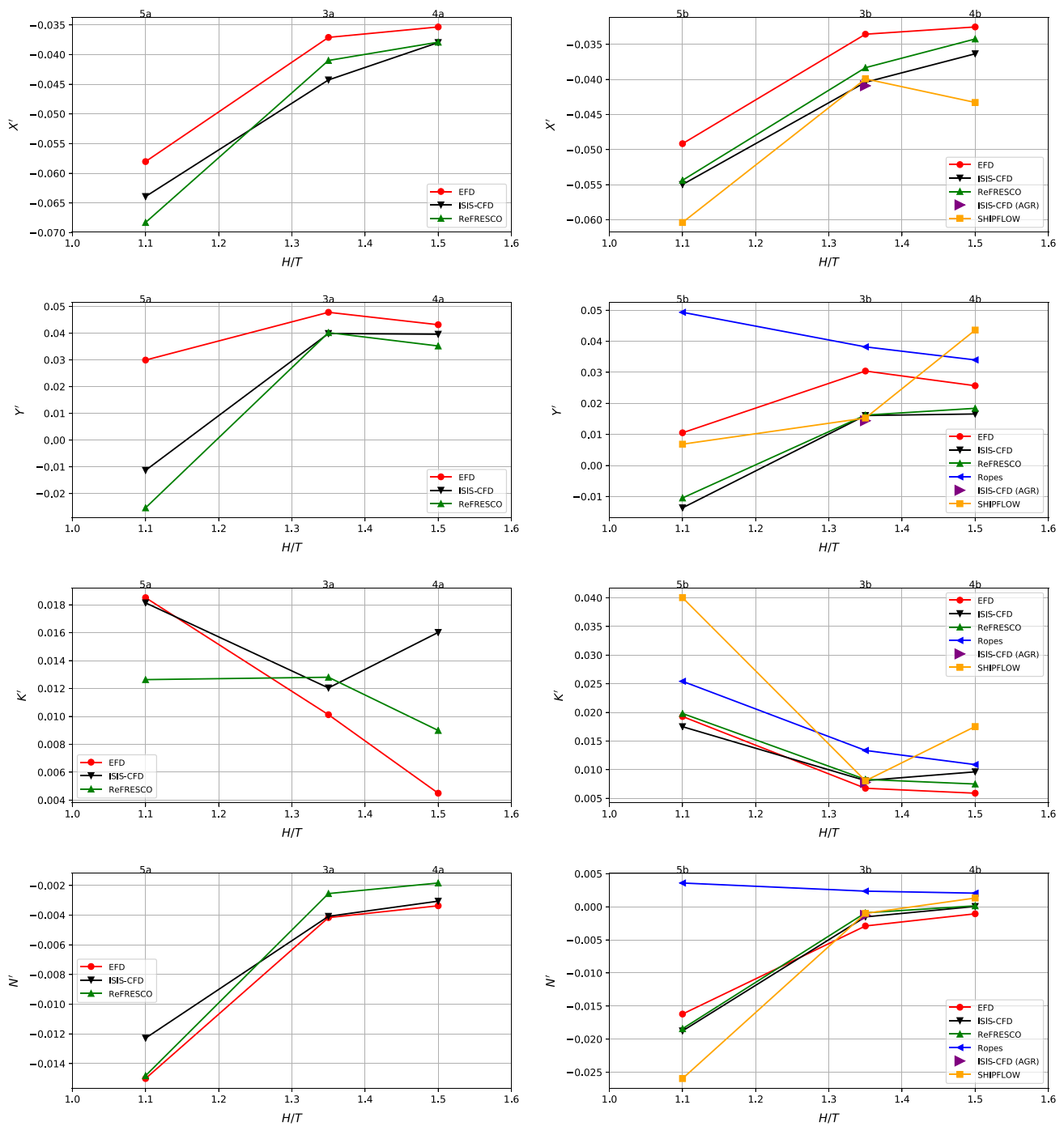
Fig. 15 Resulting forces and moments as a function of under keel clearance (left: with propulsion, right: without propulsion)

4.1 Forces and moment comparison

Qualitatively speaking, the CFD results are able to capture the trends that are present in the EFD results. Both CFD codes predict the trends in the forces and moments as a function of the distance to the bank and the under keel clearance. For example, REFRESCO and ISIS-CFD

predict that as the ship approaches the bank, the drag on the hull and the bank attraction force increase. The differences between the roll moments (K) and yawing moments (N) are small between the two CFD codes.

Quantitatively, large differences can be seen, especially for the more extreme conditions, i.e. close to the vertical wall (Fig. 14), or with small under-keel clearance
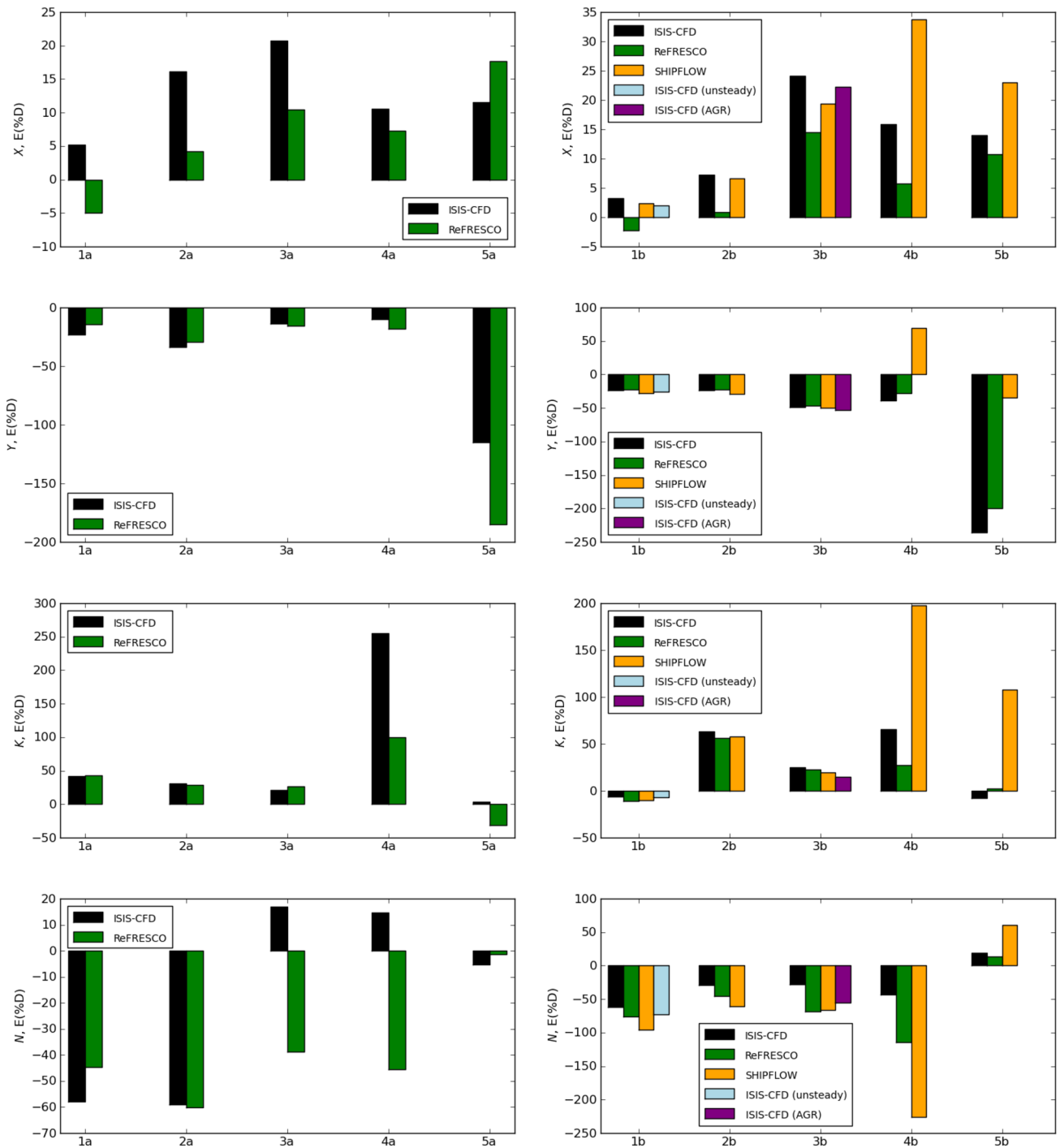
Fig. 16 Relative errors of the CFD results (left: with propulsion, right: without propulsion)

(Fig. 15). For example, REFRESCO and ISIS-CFD predict for the $H/T = 1.1$ case that the lateral force Y acts repulsive, whereas the EFD results show that for all water depths the lateral forces attracts the ship to the wall. Unfortunately, uncertainty estimates are not available for the experiments, and therefore it is not possible to conclude whether the deviations are due to modelling errors in the

CFD, or due to inaccuracies in the EFD (or both). Future work on experimental uncertainties and more in-depth CFD studies for the extreme cases is highly recommended.

The ISIS-CFD results with AGR (Figs. 14, 15) show little improvement over the results obtained using the fixed grid. The improvement is significant if a comparison is made with the results obtained on the coarse base grid

(a) K_T versus lateral position

(b) K_T versus H/T

(c) Relative error of T
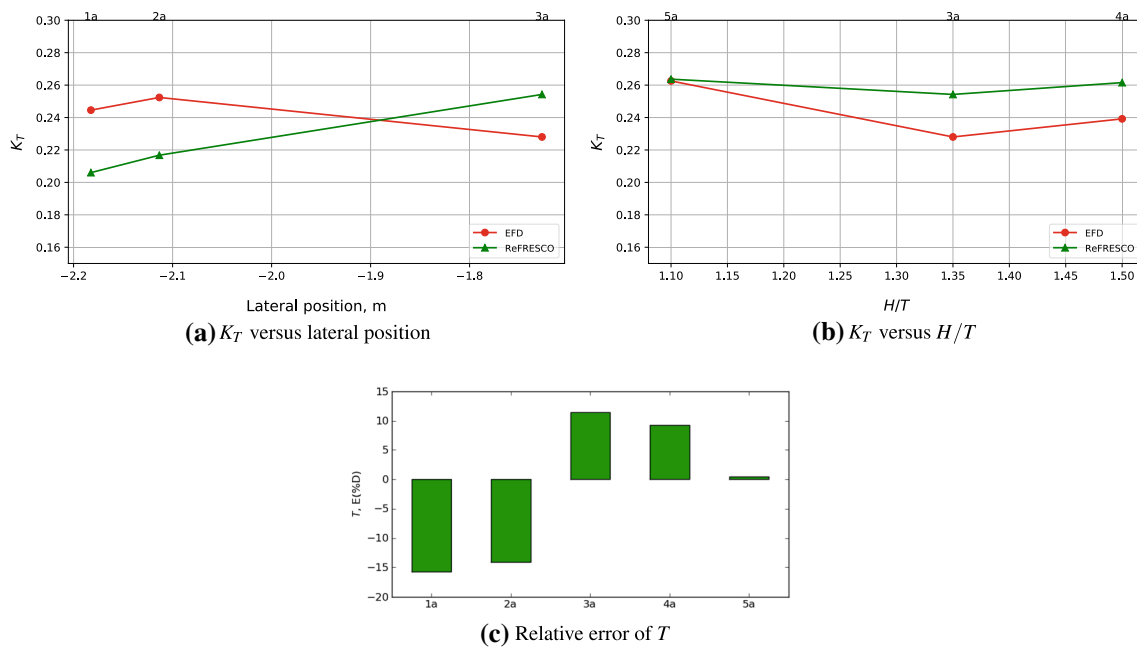
Fig. 17 Thrust computed with REFRESCO-PROCAL coupling, for given RPM of 345.3 min^{-1}

that was used as a starting point for the AGR computation (compare the results of *ISIS-CFD-c2* with those of *ISIS-CFD* (*AGR*) in Fig. 20e. From a user point

The differences between the steady and unsteady computation with ISIS-CFD for case 1b (Fig. 16) show that generally speaking, a small improvement is achieved with a second-order time discretization compared to a first-order time discretization. However, the computing time to reach a sufficiently converged solution is significantly higher for the second-order method.

ROPES predicts the wrong sign for the yawing moment (Figs. 14, 15), i.e. a moment turning the bow towards the vertical wall, instead of away from the wall as predicted by the viscous-flow codes and found during the experiments. Furthermore, the force towards the bank is considerably over-predicted. More details of the differences between the potential flow results and the viscous-flow results will be discussed in Sect. 5.8. The ROPES results have been left out of the relative comparisons (Fig. 16) due to the large errors in the absolute plots. With some exceptions (such as case 5a), the REFRESCO results are closer to the experimental values than those of ISIS-CFD or SHIPFLOW, especially for *X* and *Y*. Differences between the results for the roll and yawing moment are rather small. For case 4b, the SHIPFLOW results show errors that are significantly larger than the errors for the other contributions.

4.2 Thrust comparison

In Fig. 17, the thrust values obtained in the REFRESCO computations are presented together with the experimental values on an absolute scale, first as a function of the lateral position for case 1, 2 and 3 (Fig. 17a), and afterwards, as a function of the under keel clearance for case 3, 4 and 5 (Fig. 17b). The relative errors computed using Fig. 2 are displayed for all cases in Fig. 17c. On an absolute scale, the computed thrust values deviate no more than 0.5 Newton from the experimental values. For case 1a and 2a, the trust is under-predicted by approximately 15%, whereas for case 3a and 4a, it is predicted too high by about 11 and 9%, respectively. For case 5a, the error is less than 0.5%. In general, it is seen that the trend as a function of the water depth is reasonably captured, but not the trend due to the distance to the bank. In the present computations, no special treatment of the water depth or distance to the bank was done, and PROCAL has not been specifically developed for propellers operating in severely separating flow such as found in this study (see the discussion of the flow below). For example, it is assumed that the flow is fully attached to the propeller blade. Also the flow is assumed to leave the blade exactly at the trailing edge. These assumptions are certainly violated in a massively separated wake field and may therefore explain part of the deviations from the measurements.

Fig. 18 Hull limiting streamlines and non-dimensional shear stress as a function of distance from the vertical bank, ReFRESCO
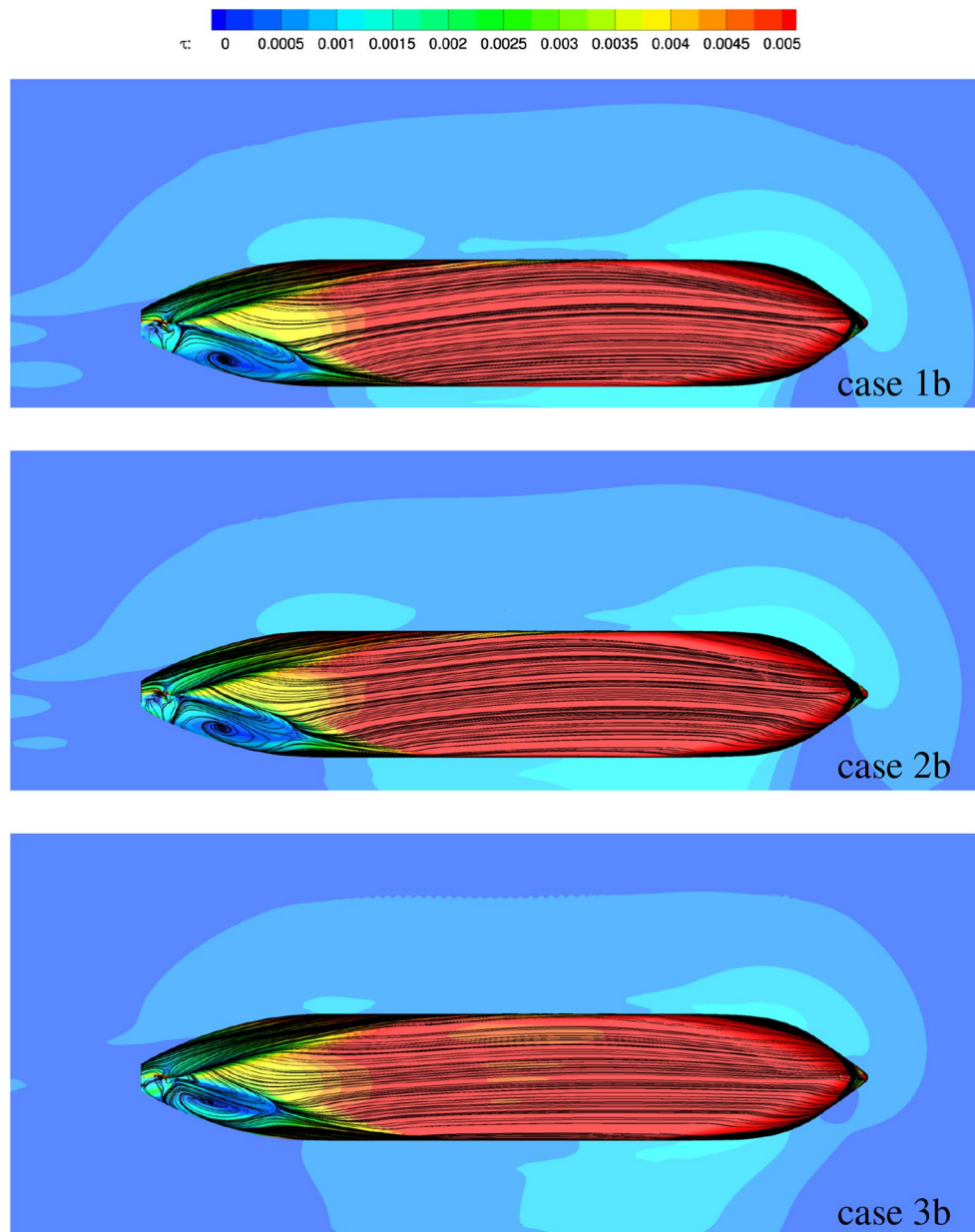

5 Comparison of local quantities

5.1 Discussion of the flow

As can be expected, the influence of the bank or bottom becomes more severe when the ship is located closer to the side wall or when the water depth reduces. In Fig. 18, the limiting streamlines on the hull and the shear stress distribution on the hull and bottom are given to illustrate the flow. For all considered cases, a stagnation point is found on the bow. Depending on the proximity of the bank, the stagnation point tends to move to the starboard (bank) side, due to the displacement effect of the hull, deflecting the flow around the hull towards port side, away from the bank, in the fore

ship area. This can be seen in the direction of the limiting streamlines aft of the bow. The flow accelerates between the vertical side of the ship and the side wall, resulting in a low pressure area and subsequently a suction force towards the bank. Just forward of midship, the limiting streamlines gradually change direction and show that the flow is directed towards the bank again in the aft area of the hull. Around the aft ship, the restriction of the flow due to the bottom and/or bank causes the flow to separate and reversal occurs. This is clearly seen in the diverging stream lines and low shear stress values at the starboard side of the aft ship. The separation also pushes the flow in the aft ship away from the bank again. In Fig. 19, the axial velocity distributions at the propeller plane (looking aft) are given for cases 1b, 3b and

Fig. 19 Axial velocity at propeller plane, REFRESCO
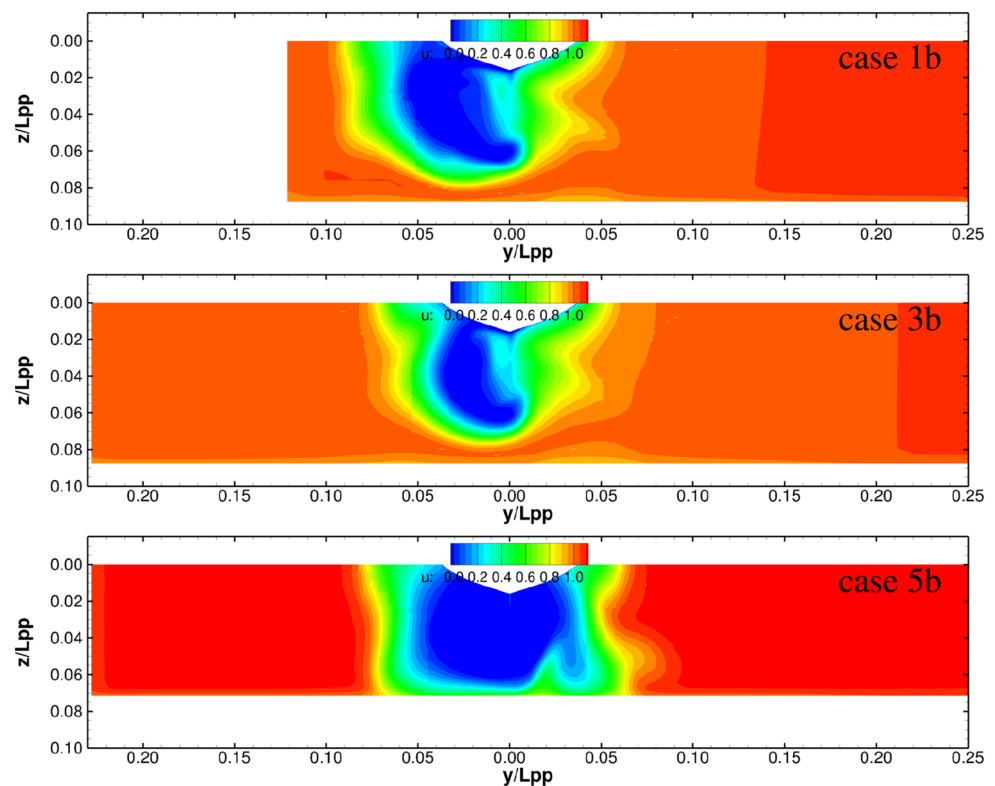
5b. In each case large areas of flow reversal are found and it is seen that these areas increase when moving closer to the wall (case 1b) or when the water depth reduces (case 5b).

5.2 Water surface elevation

For the ISIS-CFD computations, the water surface elevation was extracted along a line parallel to the quay, 0.02 m from the quay. The longitudinal coordinate is made non-dimensional using the characteristic ship length L_{pp} and an offset is applied to set the origin at the midship location. After conversion to millimetre, the results as shown in Fig. 20 are obtained for the cases with and without propulsion. For case 3b, results for a computation with adaptive grid refinement (AGR) are presented as well, these are labelled *ISIS-CFD (AGR)*. The result obtained on the base mesh that is used as a starting point for the AGR computation is given as well (*ISIS-CFD-c2*). For cases 1b, the result of a computation using a second-order time integration scheme is shown as well, this is labelled *ISIS-CFD (unsteady)*.

All computational results predict the maximum value of the trough with an error less than 1 mm. The largest errors occur for the cases with $H/T = 1.1$ (cases 5a (Fig. 20i) and 5b (Fig. 20j): the depth of the trough at the midship location is overpredicted by about 0.6 mm. The asymmetry in the depression observed for cases 2a and 2b in the experimental data is predicted with the CFD results, see Fig. 20c, d. This asymmetry is also observed for cases 1a and 1b.

For case 3b (Fig. 20f), the ISIS-CFD (AGR) result does show an improvement both in the shape of the trough and the maximum depression when compared to the coarse result from which it was started (ISIS-CFD c2): at the midship location, the error is now approximately 0.3 millimetre (this was 1.2 for the ISIS-CFD c2 result, shown in a light green colour in Fig. 20f) and the shape shows better agreement with the experimental measurement. From a user point of view, adaptive grid refinement is useful when engineering time (mesh generation) should be minimized.

5.3 Influence of distance to the bank

When the distance between the ship hull and the bank decreases, lower pressures are generated on the starboard side of the ship and therefore the suction force towards the bank increases. This can be easily seen in Fig. 21 (left), which shows the pressure distribution on the hull and channel boundaries for three different distances to the vertical wall. The lower pressure area also results in an increase of the heeling moment. The change in yaw moment as a function of the distance to the bank is less pronounced. For the smallest bank distance, it can be seen that a significant low pressure area develops at the starboard side of the bow, which results in a change of the trend of the yaw moment.
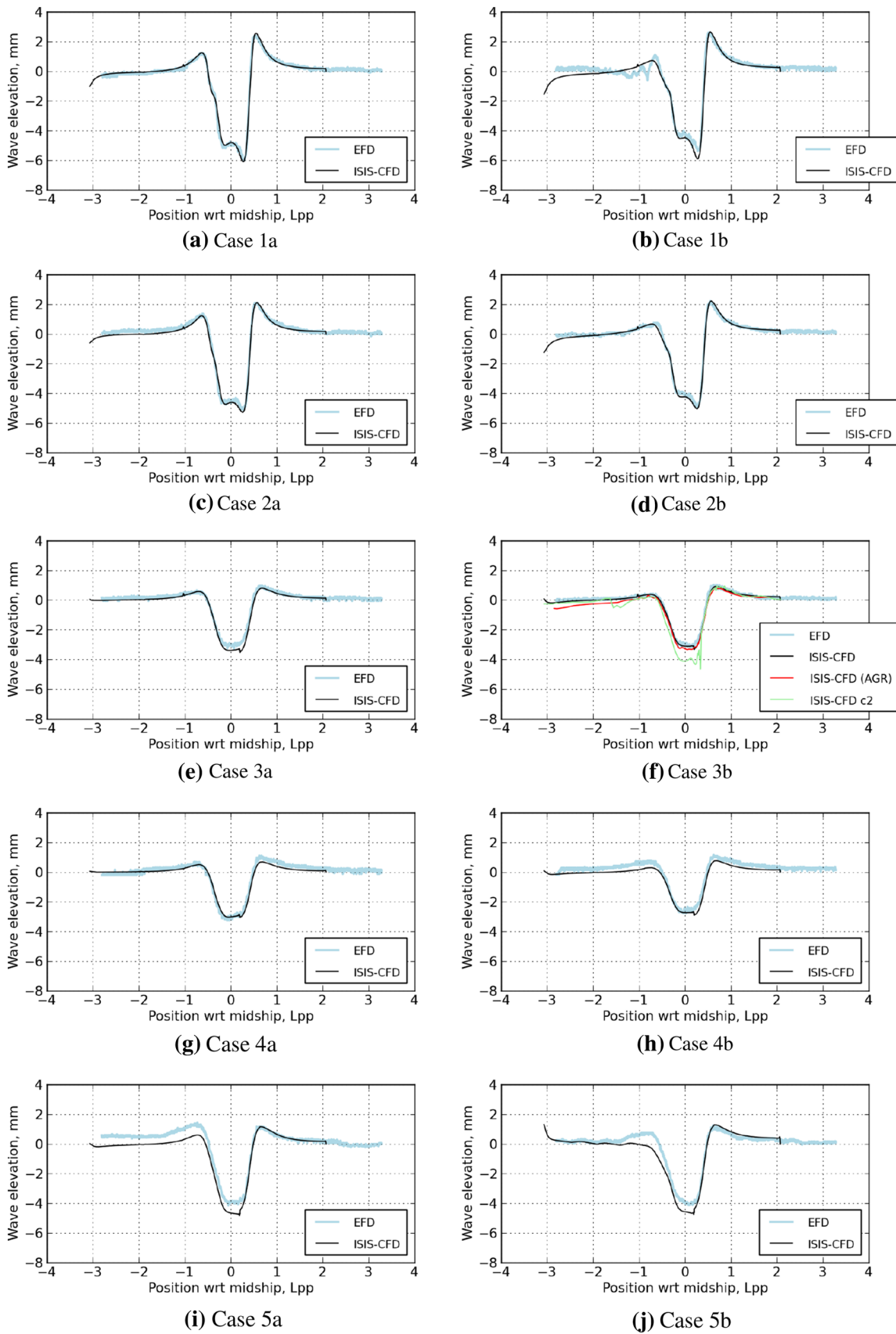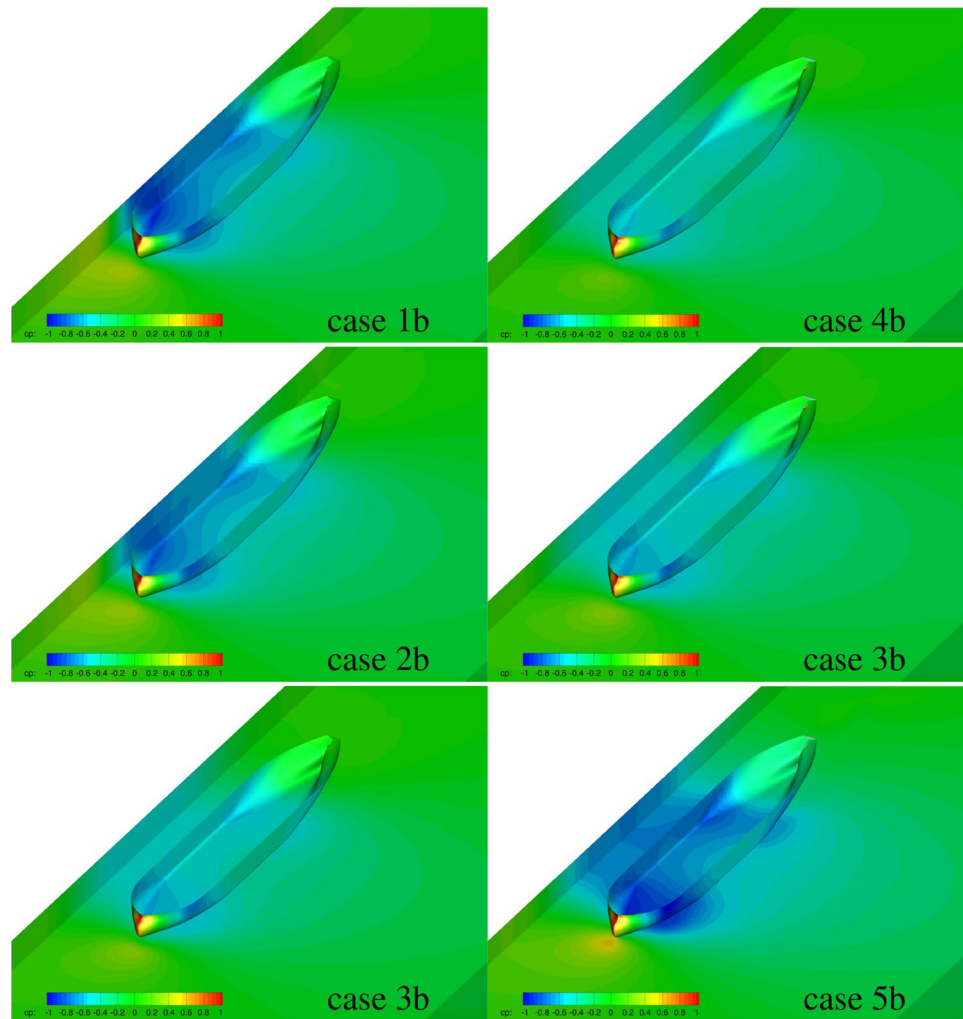
Fig. 20 Comparison of experimental and computed wave elevations (left: with propulsion, right: without propulsion)

Fig. 21 Pressure distribution on the hull and bank. Left: as a function of distance from the vertical bank, REFRESCO, right: as a function of water depth, ISIS-CFD

5.4 Influence of water depth

As expected, a smaller water depth amplifies the low pressure area on the bottom of the hull, see Fig. 21 (right). Additionally, the blockage of the flow in the channel increases and more flow separation is found around the aft ship (see also the regions with low axial velocity shown in Fig. 25 for case 3b with 35% under-keel clearance and Fig. 23 (bottom) for case 5b with 10% under-keel clearance). Due to the blockage, the flow is deflected around the model towards port side and the pressure at the port side of the model reduces. Additionally, a shift of the stagnation point on the bow to starboard is found. In the $H/T = 1.50$ case, the side force is directed to the bank, but in reduced depth conditions the low pressure area on port side and the high stagnation pressure on the starboard bow area result in a decrease of the side force. This was also found and discussed by [34]. Both ISIS-CFD and REFRESCO predict that in the $H/T = 1.1$ case the side force will even be directed away from the bank. This is however not confirmed by the measurements.

5.5 Influence of propeller

In Fig. 22 (left), the pressure distribution on the hull, vertical wall and channel bottom is compared for the case with the smallest distance to the bank with (case 1a) and without (case 1b) propeller action. It is seen that the suction of the propeller accelerates the flow in the aft ship, leading to slightly lower pressures. This results in a slightly higher side force and more negative (pulling the stern to the wall) yaw moment, see Fig. 14. Due to the propeller action, the flow does not separate as much as in the case without propeller and higher axial velocities are found in the area of the aft ship, see Fig. 22 (right). These findings agree with the conclusions from [34].

5.6 Double body vs. free surface

The computations with REFRESCO have been done under the assumption that the free surface deformation does not strongly influence the results for this specific case. In the

Fig. 22 Case 1, REFRESCO.
Top: pressure distribution on
the hull, bottom: non-dimensional axial velocity distribution
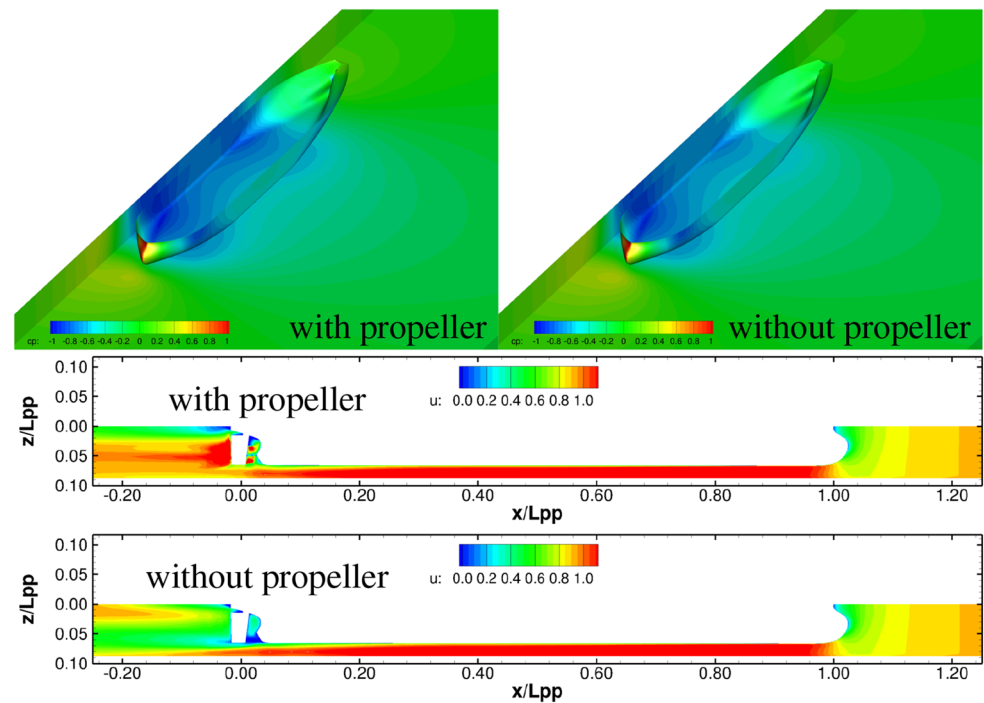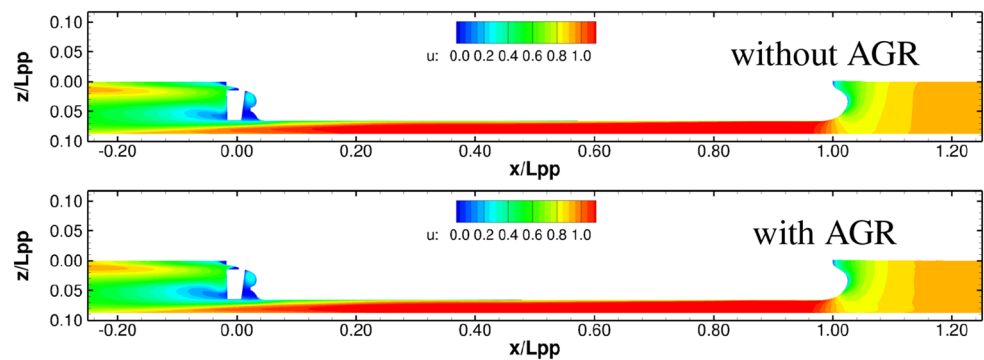at centreline ($y = 0$)

Fig. 23 Case 5b: comparison between double body
(REFRESCO) and free surface
(ISIS-CFD) modelling. Top:
pressure distribution on the hull,
bottom: non-dimensional axial
velocity distribution at centreline ($y = 0$)

ISIS-CFD computations performed by FHR and ECN/CNRS, the flow was resolved including the free surface effects. In Fig. 23, the results from REFRESCO are compared with the ISIS-CFD results obtained by FHR for case 5b. Case 5 has the smallest under-keel clearance and therefore the lowest water level in the channel and for this case the free surface effects are probably the largest, due to the largest blockage. From these figures, differences can be seen, showing especially a larger low-pressure area around midship in the double-body computation. It is therefore concluded that for this condition the free surface deformation may play a significant role. However, this case also exhibits a large area of flow separation [see the low velocity area behind the ship in Fig. 23 (right)] and this introduces instationary flow. The difference therefore may also be caused by uncertainties in the results from the different solvers.

For a less severe case, case3b, the differences between the double body approach and the approach with free surface is less pronounced, see case 3b from REFRESCO in Fig. 21 (left) and from ISIS-CFD in Fig. 21 (right). Here, only small differences can be seen, which can be caused by differences due to the solver and grid, or by the use of the free surface. It is expected that for this case, with a relatively large distance to the bank and an intermediate water depth, the influence of the free surface modelling is not significant.

5.7 Effect of automatic grid refinement

In Fig. 24 the differences in the pressure distribution obtained with the original grid and with automatic grid refinement is illustrated. Only around midship, small shifts in the contour lines are found. Also in the axial velocity distribution, see Fig. 25, only small differences can be

Fig. 24 Case 3b: pressure distribution on the hull, influence of automatic grid refinement (contour flood with white lines), compared with original grid results (black contour lines), ISIS-CFD
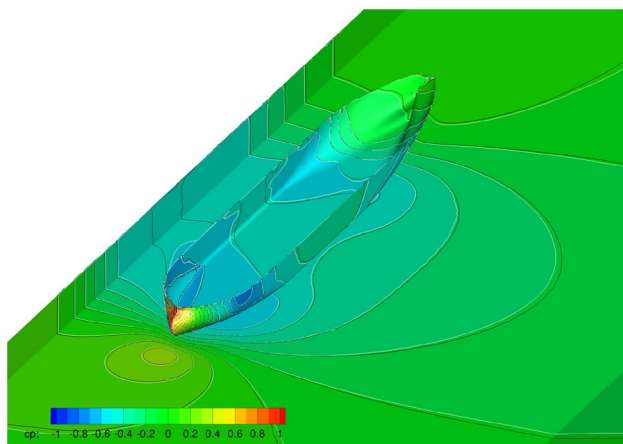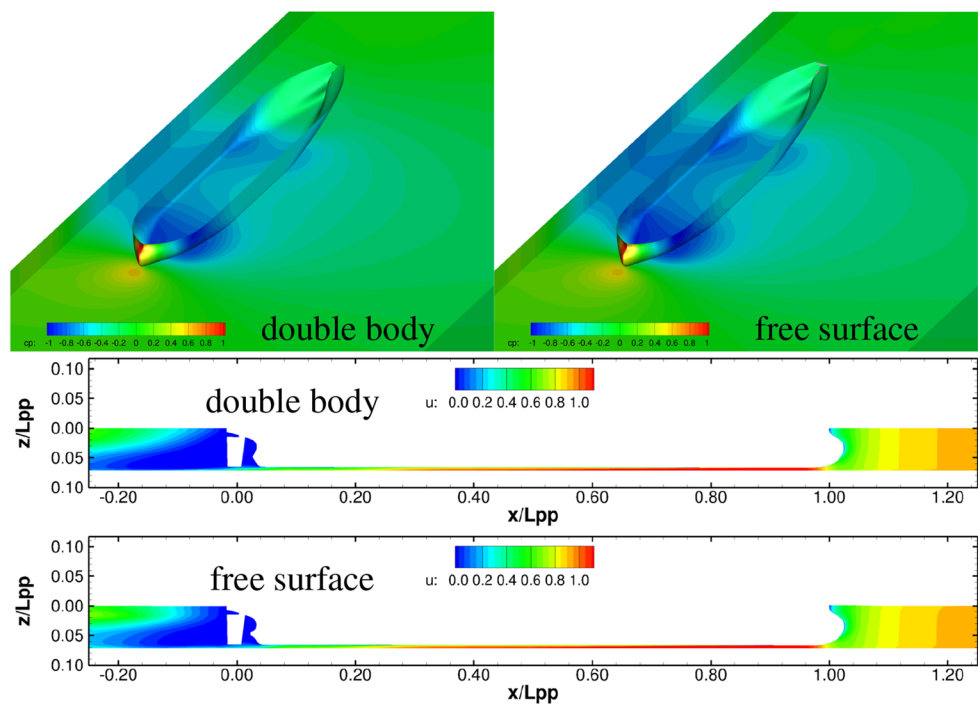

Fig. 25 Case 3b: non-dimensional axial velocity distribution at centreline ($y = 0$), influence of automatic grid refinement, ISIS-CFD
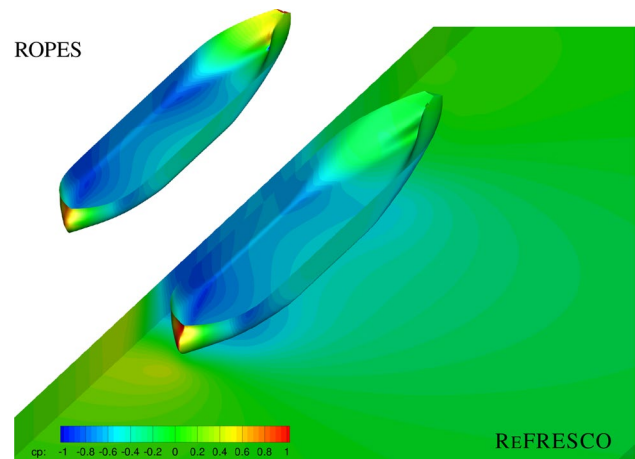

Fig. 26 Case 1b: pressure distribution on the hull, computed with ROPES (potential flow, pressure on bank and bottom has not been visualised here) and REFRESCO (viscous flow, *ultimately fine* grid)

observed. Generally, it is concluded that the automatic grid refinement does not change the flow field drastically.

5.8 Potential flow vs. viscous flow

To investigate the discrepancy of the ROPES predictions with respect to the measurements and the results for the viscous-flow predictions, the pressure distribution on the hull predicted by ROPES and by REFRESCO are compared, see Fig. 26. It is seen that on the starboard (bank-side) of the hull, lower pressures are predicted by ROPES than by REFRESCO. This results in a larger positive Y force, which

is directed towards the bank. At the forward shoulder on port side, the low pressure trough is less in ROPES than in REFRESCO. Additionally, the pressure recovery in the aft ship is much more pronounced according to ROPES. Subsequently, a higher pressure area appears to exist at the starboard side of the stern. The differences in the pressure distribution computed by ROPES will induce a larger positive yawing moment (turning the bow towards the vertical bank). These observations confirm the discrepancies found in Fig. 14. Apparently, when sailing close to a vertical bank, potential flow models will not be able to accurately

predict the bank effects, and viscous-flow methods have to be adopted to obtain the right trends of bank suction or repulsion.

6 Conclusions

This paper presents new computational results of two viscous CFD codes and one potential code for bank effects. Experimental data is used to judge the ability of the computational tools to predict bank suction effects. From a large set of experimental data, five test cases were selected where two parameters were varied: (a) the lateral distance to the bank and (b) the under keel clearance. For each test case, two experiments were available: the first one with propulsion and the second one with the propeller stopped. In total, 10 experimental conditions are used as reference. The experimental data was analysed for its statistical convergence by computing the cumulative moving average, the cumulative standard deviation and the fast Fourier transform. In general, it was found that forces and moments show better convergence than sinkage and trim values. Ideally, experimental tests used as benchmark for evaluation of CFD methods should include uncertainties in the values that are computed by repeating each test condition multiple times. This was not the case for the current experimental data set, so values without uncertainties are used for comparison. In addition to the new results presented here, CFD results from literature are shown in the comparisons as well.

The grid convergence studies with REFRESCO and ISIS-CFD show that in order to obtain sufficiently low discretization errors, very fine grids (with or without automatic grid refinement) are required.

Based on comparisons of the computations with experimental results, it is found that bank effects can be predicted using CFD tools. However, some deviation from the measurement is seen and this needs further study. Using other turbulence models may affect the results. Although the ISIS-CFD results with adaptive grid refinement indicate that improvements may be possible, other parameters need to be investigated as well. The majority of computations presented here were computed in steady mode. For the computations that were executed in unsteady mode, small but insignificant improvements were observed in the integral quantities. Comparisons of local flow quantities have shown unsteady flow behaviour, but the time-averaged differences between steady and unsteady computations are small. However, further studies to investigate e.g. the influence of the step size and convergence settings per step on the results and better control of the statistical convergence of the solutions are recommended to see if better agreement between the CFD and EFD can be obtained. Additionally, more insight into the

experimental uncertainties is required in order to be able to validate the results.

The effect of the propeller amplifies the bank effects, due to the reduction of pressures in the aft ship area and due to a change of the separation of the flow around the stern. To fully predict bank effects the propeller should therefore be incorporated in the computations. For the cases considered in this study, it is found that the consideration of free surface deformation does not significantly influence the predicted forces and moments, except for very small under keel clearance values.

The study also shows that for sailing close to a vertical bank in shallow water, potential flow models are not able to accurately predict the bank effects, and viscous-flow methods have to be adopted to obtain the right trends of bank suction or repulsion.

References

1. Bunnik THJ, Toxopeus SL (2011) Viscous flow effects of passing ships in ports. In: 30th International Conference on Ocean, Offshore and Arctic Engineering (OMAE), OMAE2011-49519. Rotterdam, The Netherlands. https://doi.org/10.1115/OMAE2011-49519

2. Chen HC, Liut DA, Hwang WY, Lin WM (2003) An advanced viscous flow computation method for ship–ship dynamic interactions in shallow and restricted waterway. In: International Conference on Marine Simulation and Ship Manoeuvring (MARSIM). The Society of Naval Architects of Japan and Japan Institute of Navigation, Kanazawa, Japan, pp RC–35–1–10

3. Dacles-Mariani J, Zilliac GG, Chow JS, Bradshaw P (1995) Numerical/experimental study of a wingtip vortex in the near field. AIAA J 33(9):1561–1568. https://doi.org/10.2514/3.12826

4. Dand IW (1981) On ship–bank interaction. In: RINA Spring Meeting

5. Delefortrie G (2015) Accuracy of measurement devices for sinkage at the Flanders Hydraulics Research shallow-water towing tank

6. Deng GB, Queutey P, Vissonneau M, Salvatore F (2013) Ship propulsion prediction with a coupled RANSE-BEM approach. In: Brinkmann B, Wriggers P (eds) The V International Conference on Computational Methods in Marine Engineering. Marine 2013

7. Deng GB, Visonneau M (1999) Comparison of explicit algebraic stress models and second-order turbulence closures for steady

flow around ships. In: 7th Symposium on Numerical Ship Hydrodynamics. 10.1.1.534.5953

8. Eça L, Hoekstra M (2009) Evaluation of numerical error estimation based on grid refinement studies with the method of the manufactured solutions. Comput Fluids 38(8):1580–1591. https://doi.org/10.1016/j.compfluid.2009.01.003

9. Eça L, Hoekstra M (2014) A procedure for the estimation of the numerical uncertainty of CFD calculations based on grid refinement studies. J Comput Phys 262:104–130. https://doi.org/10.1016/j.jcp.2014.01.006

10. Guilmineau E, Chikhaoui O, Deng GB, Visonneau M (2013) Cross wind effects on a simplified car model by a DES approach. Comput Fluids 78:29–40. https://doi.org/10.1016/j.compfluid.2011.08.020

11. Klaij CM, Vuik C (2013) SIMPLE-type preconditioners for cell-centered, colocated finite volume discretization of incompressible Reynolds-averaged Navier–Stokes equations. Int J Num Methods Fluids 71(7):830–849. https://doi.org/10.1002/fld.3686

12. Korsmeyer FT, Lee CH, Newman JN (1993) Computation of ship interaction forces in restricted waters. J Ship Res 37(4):298–306

13. Lataire E, Vantorre M, Delefortrie G (2012) A prediction method for squat in restricted and unrestricted rectangular fairways. Ocean Eng 55(55):71–80. https://doi.org/10.1016/j.oceaneng.2012.07.009

14. Leroyer A, Visonneau M (2005) Numerical methods for RANSE simulations of a self-propelled fish-like body. J Fluids Struct 20:975–991. https://doi.org/10.1016/j.jfluidstructs.2005.05.007

15. Lo DC, Su DT, Lin IF (2009) Applying computational fluid dynamics to simulate bank effects. In: Nineteenth International Offshore and Polar Engineering Conference. Osaka, Japan, pp 466–471

16. Menter FR, Egorov Y (2005) A scale-adaptive simulation model using two-equation models. In: 43rd AIAA Aerospace Sciences Meeting and Exhibit, AIAA 2005-1095. American Institute of Aeronautics and Astronautics, Reno, Nevada

17. Menter FR, Kuntz M, Langtry R (2003) Ten years of industrial experience with the SST turbulence model. In: Fourth International Symposium on Turbulence. Heat and Mass Transfer. Antalya, Turkey, pp 625–632

18. Pereira FS, Vaz G, Eça L (2015) An assessment of Scale-Resolving Simulation models for the flow around a circular cylinder. In: 8th International Symposium on Turbulence, Heat and Mass Transfer (THMT'15). Sarajevo, Bosnia and Herzegovina

19. Pinkster JA (2004) The influence of a free surface on passing ship effects. Int Shipbuild Prog 51(4):313–338

20. Pinkster JA, Bhawsinka K (2013) A real-time simulation technique for ship–ship and ship–port interactions. In: The 28th international Workshop on Water Waves and Floating Bodies (IWWWFB). L'Isle sur la Sorgue, France

21. Queutey P, Visonneau M (2007) An interface capturing method for free-surface hydrodynamic flows. Comput Fluids 36:1481–1510. https://doi.org/10.1016/j.compfluid.2006.11.007

22. Rijpkema DR, Starke AR, Bosschers J (2013) Numerical simulation of propeller–hull interaction and determination of the effective wake field using a hybrid RANS-BEM approach. In: Third International Symposium on Marine Propulsors (SMP). Launceston, Tasmania, Australia

23. Tuck EO, Newman JN (1974) Hydrodynamic interactions between ships. In: 10th Symposium on Naval Hydrodynamics. Office of Naval Research, pp 35–51

24. Van Kerkhove G, Vantorre M, Delefortrie G (2009) Advanced model testing techniques for ship behaviour in shallow and confined water. In: Proceedings of AMT. http://www.vliz.be/imisdocs/publications/153758.pdf

25. Vantorre M, Laforce E (1998) Experimental investigation of hydrodynamic forces acting on a ship in the vicinity of a quay wall. In: MAN'98 International Symposium and Workshop on Forces Acting on a Manoeuvring Vessel. Val de Reuil, France

26. Vaz G, Bosschers J (2006) Modelling of three dimensional sheet cavitation on marine propellers using a boundary element method. In: Sixth International Symposium on Cavitation (CAV). Wageningen, The Netherlands

27. Vaz G, Jaouen FAP, Hoekstra M (2009) Free-surface viscous flow computations. Validation of URANS code FreSCo. In: 28th International Conference on Ocean, Offshore and Arctic Engineering (OMAE), OMAE2009-79398. Honolulu, Hawaii. https://doi.org/10.1115/OMAE2009-79398

28. Wackers J, Deng GB, Leroyer A, Queutey P, Visonneau M (2014) Combined refinement criteria for anisotropic grid refinement in free-surface flow simulation. Comput Fluids 92:209–222. https://doi.org/10.1016/j.compfluid.2013.12.019

29. Wackers J, Deng GB, Leroyer A, Queutey P, Visonneau M, Palmieri A, Liverani A (2015) Can adaptive grid refinement produce grid-independent solutions for complex flows? In: Chinesta F, Chamoin L, Diez P (eds) VII International Conference on Adaptive Modeling and Simulation

30. Xiang X, Faltinsen OM (2010) Maneuvering of two interacting ships in calm water. In: 11th International Symposium on Practical Design of Ships and Other Floating Structures (PRADS). Rio de Janeiro, Brazil

31. Yeung RW, Tan WT (1980) Hydrodynamic interactions of ships with fixed obstacles. J Ship Res 24(1):50–59

32. Zhou M, Zou Z (2013) Numerical study on the influences of canal geometry on ship squat. Sci J Maritime Univ Szczecin 36(1):5. http://repository.am.szczecin.pl/handle/123456789/554

33. Zou L (2012) CFD predictions including verification and validation of hydrodynamic forces and moments on ships in restricted waters. Ph.D. thesis, Chalmers University of Technology, Department of Shipping and Marine Technology, Gothenburg, Sweden

34. Zou L, Larsson L (2013) Confined water effects on the viscous flow around a tanker with propeller and rudder. Int Shipbuild Prog 60(1–4):101–125. https://doi.org/10.3233/ISP-130101

35. Zou L, Larsson L, Delefortrie G, Lataire E (2011) CFD prediction and validation of ship–bank interaction in a canal. In: 2nd International Conference on Ship Manoeuvring in Shallow and Confined Water: Ship to Ship Interaction. Trondheim, Norway